Development of permeable networks by viscous-brittle deformation in a shallow rhyolite intrusion. Part 1: Field evidence

Taylor Witcher, Steffi Burchardt, Tobias Mattsson, Michael Heap, William Mccarthy

Journal of Volcanology and Geothermal Research 454 (2024) 108166

Contents lists available at ScienceDirect

Journal of Volcanology and Geothermal Research

journal homepage: www.journals.elsevier.com/journal-of-volcanology-and-geothermal-research

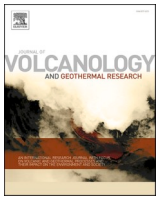

Development of permeable networks by viscous-brittle deformation in a shallow rhyolite intrusion. Part 1: Field evidence

Taylor Witcher [a,b,*], Steffi Burchardt [a,b], Tobias Mattsson [a,c,d], Michael J. Heap [e,f], William McCarthy [c]

[a] Department of Earth Sciences, Uppsala University, Uppsala, Sweden
[b] Centre for Natural Hazards and Disaster Science, Sweden
[c] School of Earth and Environmental Sciences, University of St. Andrews, Bute Building, Queen's Terrace, KY16 9TS St Andrews, UK
[d] Department of Geological Sciences, Stockholm University, Svante Arrhenius väg 8, 114 18 Stockholm, Sweden
[e] Université de Strasbourg, CNRS, Institut Terre et Environnement de Strasbourg, UMR 7063, 5 rue Descartes, Strasbourg F-67084, France
[f] Institut Universitaire de France (IUF), Paris, France

ARTICLE INFO

Keywords:
Rhyolite deformation
Laccolith emplacement
Magma fracture
Permeability
Outgassing
Sandfell

ABSTRACT

Efficient outgassing of shallow magma bodies reduces the risk of explosive eruption. Silica-rich magmas are too viscous for exsolved gas bubbles to escape the system through buoyant forces alone, and so volatile overpressure is often released through deformation-related processes. Here we present a case study on magma emplacement-related deformation in a shallow (~500 m depth) rhyolite intrusion (the Sandfell laccolith, Eastern Iceland) to investigate the establishment of degassing (volatile exsolution) and outgassing (gas escape) networks in silicic sub-volcanic intrusions. We observe viscous and brittle deformation features: from vesiculated flow bands that organized into 'pore channels' in the ductile regime, to uniform bands of tensile fractures ('fracture bands') that grade into breccia and gouge in the brittle regime. Through field mapping, structural analysis, and anisotropy of magnetic susceptibility (AMS) measurements, we show that areas with higher degrees of brittle deformation are proximal to abruptly changing AMS fabrics, and flow band orientations and point to laccolith-wide strain partitioning in the magma. We associate the changes in flow fabrics and the intensity of brittle deformation to the transition from dominantly horizontally flowing magma during initial sill-stacking to up to the NE magma flow linked to the propagation of a trap-door fault from the N to the SE. The establishment of intrusion-scale brittle permeable networks linked to changes in strain partitioning that facilitated magma flow during different stages of laccolith growth would have profoundly assisted the outgassing of the entire laccolith. Magmatic fracturing captures viscous and brittle processes working in tandem as an efficient outgassing mechanism, and should be considered in sub-volcanic intrusions elsewhere.

1. Introduction

Magma intruding at shallow depths can pose risks of cataclysmic eruption due to, for instance, pressure build-up from magma degassing (Tait et al., 1989; Clocchiatti et al., 1994; Rooyakkers et al., 2021). However, in some cases, such shallow magma bodies remain unerupted and simply solidify in place—for example, a laccolith that grew during the 2011 eruption of Cordón Caulle, Chile (Castro et al., 2016). Following explosive eruption and synchronous with rhyolite lava effusion at Cordón Caulle, surface deformation recorded >200 m of uplift near the vent in a matter of days, which was interpreted as a shallow magmatic intrusion. Such rapid intrusion rates are alarming, and an explosive eruption would seem likely if the magmatic gasses had no escape. However, no cataclysmic explosion followed, only outgassing around the vent and ~ 40 m subsidence (Castro et al., 2016). So, what determines magma eruptibility at shallow depths, and what controls explosivity when magma does erupt?

Magma is a complex material, usually consisting of liquid silicate melt, gas bubbles, and solid crystals. The proportion of crystals, concentration of volatiles, and silica content of the melt affects a magma's resistance to flow, i.e. its viscosity (Hess and Dingwell, 1996; Giordano et al., 2004a; Giordano et al., 2004b). When undergoing shear (e.g.,

* Corresponding author at: Department of Earth Sciences, Uppsala University, Uppsala, Sweden.
E-mail address: taylor.witcher@geo.uu.se (T. Witcher).

https://doi.org/10.1016/j.jvolgeores.2024.108166
Received 18 December 2023; Received in revised form 5 August 2024; Accepted 13 August 2024
Available online 15 August 2024

when intruding), a magma with low viscosity flows, because the silicate melt is able to dissipate applied stress through viscous relaxation (Dingwell and Webb, 1989). With increasing viscosity and/or applied strain rate, magma will exhibit non-Newtonian behavior, following Maxwell's viscoelasticity model (Webb and Dingwell, 1990; Dingwell, 1996; Wadsworth et al., 2019). When strain rates are high, the silica network of the melt is not able to reorient quickly enough and will instead sustain fracture nucleation and growth when stresses exceed the strength of the melt (Webb and Dingwell, 1990; Dingwell, 1996; Tuffen et al., 2008). Once the stress is released through brittle failure, the liquid relaxes and heals, and can erase all evidence of fracturing. This phenomenon in silicate melts has been thoroughly investigated in laboratory settings (Dingwell and Webb, 1989; Dürig and Zimanowski, 2012; Lavallée et al., 2012; Kushnir et al., 2017; Wadsworth et al., 2018; Lamur et al., 2019), and results of its occurrence in nature are recorded in ash-generating eruptions (Cashman and Scheu, 2015; Gardner et al., 2017; Giachetti et al., 2021) and features known as 'tuffisites'. Tuffisites occur when magma fractures and exsolved volatiles and pyroclasts fill the void before it welds shut (Tuffen et al., 2003; Saubin et al., 2016; Unwin et al., 2021). The presence of crystals or bubbles in the melt alters the strength of the magma, generally allowing for brittle failure at lower bulk strain rates than pure melt (Cordonnier et al., 2012; Pistone et al., 2015).

During magma ascent, the exsolution of volatiles (e.g., H_2O, CO_2, SO_2) introduces gas bubbles into the melt (degassing) that impart stress on the surrounding melt as they grow (Sparks, 2003). In low-viscosity

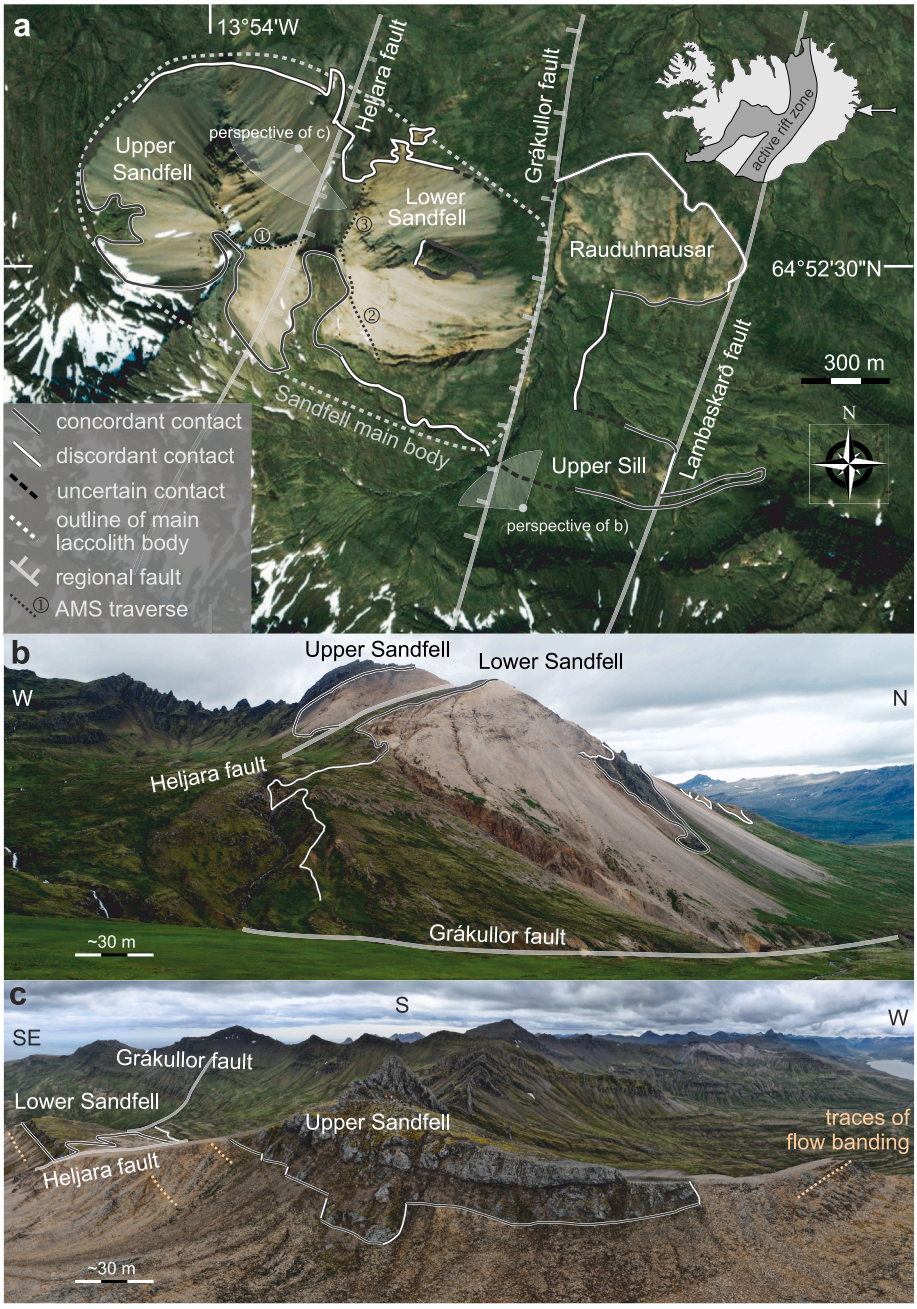

Fig. 1. a) Map view of the Sandfell laccolith main body and Rauduhnausar and Upper Sill intrusions, as mapped by Mattsson et al. (2018). Satellite image: June 2009, Maxar Technologies through Google Earth Pro. The location of the Sandfell laccolith in relation to the active rift zone is indicated in the inset map of Iceland (with the white arrow). b) Ground view of Upper and Lower Sandfell, with contacts with basalt lava host rocks visible. c) Photosphere image (360-degree photograph) of the peak of Upper Sandfell, and the complex roof rock-intrusion relationships. Note traces of flow banding.

magma, bubbles can usually grow and ascend, decoupling from the magma and escaping the system (outgassing) through coalescence, diffusion, and decompression (Parfitt and Wilson, 2008). However, rapid decompression can cause bubbles to grow quickly, faster than the relaxation timescale of the melt, and thus imposing stress that exceeds the tensile strength, which results in fractures propagating away from the bubble wall into the melt (Alidibirov and Dingwell, 1996; Kameda et al., 2008). If bubbles nucleate close together and those discrete fractures meet a neighboring bubble, the pressures combine and drive further fracturing which can initiate the runaway process of bulk magma fragmentation (Papale, 1999; Gonnermann and Manga, 2009). This process can generate the impressive ash columns of explosive Vulcanian or Plinian eruptions. Bulk fragmentation can occur in a rapidly ascending magma body (Burgisser and Gardner, 2004; Gonnermann and Manga, 2009), following the collapse of a lava dome (Mt Unzen 1991, Japan: Sato et al., 1992), or the sudden unloading of an overburden via landslide or sector collapse (e.g., Mt. St Helens 1980, USA; Moore and Rice, 1984). However, in many cases, volatiles find a way to escape into the atmosphere or surrounding host rock without bulk fragmentation: through permeable networks in the magma body (Rust and Cashman, 2004; Okumura et al., 2010; Heap et al., 2019b; Ryan et al., 2019; Crozier et al., 2022). How and when these permeable outgassing pathways form can determine the fate of a high-viscosity magma body.

Even during magma emplacement within the volcanic plumbing system, stresses caused by prolonged shearing of high-viscosity magma should frequently exceed the tensile and shear strength of the magma. As a consequence, magma outgassing may be substantial due to viscous and brittle processes working in tandem. Here, we present a rare case study with a range of excellently preserved deformation features, spanning both the viscous and brittle regime in a 'deformation spectrum': the Sandfell laccolith in Eastern Iceland (Fig. 1). We investigate (1) what the deformation features tell us about magma emplacement dynamics, (2) whether these deformation features allowed for magma outgassing, and (3) implications for these outgassing mechanisms in high-viscosity intrusions.

We present the results of structural field mapping, anisotropy of magnetic susceptibility (AMS) measurements, and strain analysis to highlight evidence for the link between magma emplacement-related strain distribution and outgassing style. The different types of deformation in this study are categorized based on field observations combined with macro- and microscale textural analyses. The associated microanalysis of the deformation features can be found in the companion paper (Witcher et al., *submitted*). Our results show how the magma degassed through viscous processes and outgassed sequentially through brittle mechanisms during emplacement, which ultimately prevented an eruption.

2. Geological setting

The rhyolitic Sandfell laccolith is situated in Fáskruðsfjörður on Iceland's East coast (Fig. 1). Its formation is associated with a silicic phase of the Neogene rift-zone volcanism of the Reydarfjörður central volcano (Gibson et al., 1966; Martin et al., 2011). Zircons from the Sandfell laccolith have been dated by both Martin et al. (2011) and Padilla (2015) and yielded $^{40}Ar/^{39}Ar$ ages of 11.7 +/− 0.1 Ma and U/Pb ages of 11.9 +/− 0.12 Ma, respectively. Rhyolite magma initially intruded along a regionally extensive layer of ignimbrite (named T2) below 540 m of predominantly basaltic lava deposits (Hawkes and Hawkes, 1933; Mattsson et al., 2018), likely as a pyroclastic sill (Unwin et al., 2021). The sill then inflated into a dome-shaped laccolith, about 500 m thick, which is connected to two sill-like offshoots, called Rauduhnausar and the Upper Sill (Mattsson et al., 2018). Space for the emplacement of the 0.57 km^3 of rhyolite magma was created by uplift and doming of the overlying basalt lava pile, which created both concordant laccolith-host rock contacts, as well as faulted, discordant contacts, particularly in the North (Fig. 1; Mattsson et al., 2018). Together with the entire region, the Sandfell laccolith and its host rocks were later tilted by about 10–15° to the WNW and the active rift zone (Óskarsson and Riishuus, 2013).

Three steeply-dipping regional normal faults crosscut the Sandfell laccolith (Fig. 1). The Heljara and Grákullor faults formed a graben that displaced the center of the Sandfell laccolith (Lower Sandfell mountain) downward by 70 to 120 m (Gibson, 1963). Faulting likely occurred after the laccolith was emplaced since the parts of the laccolith within and outside the graben are located at the same stratigraphic position. No evidence suggests the magma was influenced by the faults, such as intensified hydrothermal alteration along the fault plane, magmatic textural heterogeneity surrounding the fault, and/or diking of the magma into the roof rock along the fault. However, the Lambaskarð fault is interpreted as a *syn*-magmatic structure that influenced the emplacement and geometry of the Rauduhnausar and Upper Sill intrusions (Fig. 1a; see also Mattsson et al., 2018).

The Sandfell rhyolite is an oligoclase porphyry (~5% phenocrysts) with a microcrystalline groundmass. A systematic fracture network is preserved in the rhyolite, consisting of cm- to dm-scale tensile fractures arranged in bands in nearly every outcrop. Drone photos of the northern peak of the laccolith show traces of sub-horizontal layering, which abruptly disappear in the underlying rhyolite (Fig. 1c). Samples collected near the contact with basalt host rock are darker in color and more aphanitic. Other than these observations, the rhyolite lacks any distinct chilled margins. Mattsson et al. (2018) concluded that these observations imply a rapid successive or continuous intrusion process over a 2 to 18-year period, as modeled based on silicic extrusive rates in Iceland. The magma type and proposed rapid emplacement timescale greatly increased the probability of the Sandfell laccolith erupting. However, no silicic eruptive deposits occur in the exposed locations of the palaeosurface of the time when the Sandfell laccolith formed. Moreover, no vent structures were observed within the laccolith. Here, we test the hypothesis that pervasive outgassing by brittle magma deformation depressurized the system sufficiently to avoid a catastrophic eruption of the Sandfell laccolith.

3. Methods

3.1. Field mapping

During a field campaign in August 2021, we systematically mapped all accessible outcrops in the main part of the Sandfell laccolith, i.e. excluding the Upper Sill and the Rauduhnausar offshoots (Fig. 1). We mapped 106 outcrops using the FieldMOVE Clino application on an Apple iPhone 7 and documented each outcrop with photographs and structural measurements. Photos taken through FieldMOVE Clino were georeferenced in real-time during the field campaign, and those that were taken with a Nikon Z6II camera were referenced using time stamps and two constraining georeferenced photos. We recorded flow banding and the occurrence of vesicles and fractures. We used the FieldMOVE Clino application to measure the strike and dip of flow bands, fracture bands, and the fractures within them. The application was calibrated to the local magnetic declination. We recalibrated the iPhone compass frequently and tested its accuracy with a geologic compass every ca. 10 measurements, they were always within a 1° error. Due to the anastomosing nature of the flow bands and fracture bands, measurements were only taken when we were confident the orientation was representative. In other words, only consistently planar features with reproducible strike and dip were measured. Moreover, we defined qualitative categories of outcrop deformation based on mapping and photography (see Section 4).

In addition to field mapping, we used unmanned aerial vehicle (UAV, i.e., drone) images to aid the extrapolation of our observations to inaccessible areas and measure the thickness of large-scale features. To correlate ground observation sites with the internal structure of the laccolith at non-accessible locations, we also took UAV images (5472 ×

3648 pixels) with a DJI Mavic 2 Pro along Transect 1 at about a 10-m distance from the outcrop. In total 787 photos were processed with structure-from-motion photogrammetry in Agisoft Metashape to produce a tiled virtual outcrop model with a tile size of 256 pixels in 11 levels. Image overlap was generally ≥9 across the virtual outcrop model area (see Supplementary Material 1 for model survey statistics and image locations). In addition, 16 aerial images were taken and provided by Birgir Oskarsson, Icelandic Institute of Natural History, in 2011. They were used to produce an overview model of the main body of the laccolith. The planar flow features within the rhyolite were measured as lines on the Transect 1 virtual outcrop in the software Agisoft Viewer. The lines were imported into MOVE 2022 by PETEX to convert 3D line vertices to planar features with extractable orientations.

3.2. Structural analysis in MOVE

We used the 3D reconstruction of the Sandfell laccolith created by Mattsson et al. (2018) in the Petex© MOVE software as a base for our structural analysis. Plotting the observed degree of deformation on the 3D map and correcting for the post-emplacement displacement along the Heljara fault (75–120 m; Gibson, 1963), allowed us to correlate features on Upper and Lower Sandfell so we could analyze structural measurements and observations based on distance from the laccolith-host rock contact.

3.3. Anisotropy of magnetic susceptibility (AMS)

Since AMS commonly reflects the shape and/or distribution fabric of ferrimagnetic minerals in magmatic rocks (Hargraves et al., 1991; Stephenson, 1994; Grégoire et al., 1998; Rochette et al., 1999; Gaillot et al., 2006; Borradaile and Jackson, 2010; Mattsson et al., 2021), it acts as a proxy for the strain associated with the magma flow prior to viscous stagnation and fracturing of the magma. In order to identify the orientation of flow-related fabrics and differences in magmatic strain within the densely fractured areas of the Sandfell laccolith, we employed high-density sampling of oriented block samples along three transects in the main body of the Sandfell laccolith: The transects are located (i) along the ridge between Upper and Lower Sandfell, representing the fault scarp of the Heljara fault; (ii) on the south side of Lower Sandfell, and (iii) on the north side of Lower Sandfell (Fig. 4). We drilled cores of ~25 mm diameter and 22 mm length from each block sample with a drill press using a non-magnetic diamond tip abrasive core bit. The core specimens were reoriented to their declination-corrected geographic coordinate system for the interpretation of the AMS data.

Low-field in-phase AMS was measured on each sub-specimen with a KLY-5 Kappabridge in a field of 400 A/m and with a frequency of 1440 Hz using a 3D automatic spinning specimen holder. A mean symmetric second-rank magnetic susceptibility tensor was calculated using the least square inversion method of Jelínek (1978). The magnetic susceptibility tensor defines the length and orientation of the three orthogonal, principal axes of susceptibility, $k_1 \geq k_2 \geq k_3$, which can be visualized as an ellipsoid (Khan, 1962). Tarling and Hrouda (1993) summarize parameters used to describe magnetic fabrics. The mean magnetic susceptibility (K_m) is given by:

$$K_m = \frac{k_1 + k_2 + k_3}{3}.$$

The parameters P_j, and T (Jelínek, 1981) describe the corrected degree of anisotropy and the shape of anisotropy of the AMS ellipsoid, respectively. The corrected degree of anisotropy is defined as:

$$P_j = exp\sqrt{2\left((\eta_1 - \eta_m)^2 + \left(\eta_2 - \eta_m\right)^2 + (\eta_3 - \eta_m)^2\right)}$$

where $\eta_x = ln(k_x), x = 1, 2, 3$ and

$$\eta_m = \frac{\eta_1 + \eta_2 + \eta_3}{3}$$

Pj values larger than 1 define an anisotropic fabric. The shape (T) parameter is given by:

$$T = \frac{2\eta_2 - \eta_1 - \eta_3}{\eta_1 - \eta_3}.$$

The magnetic susceptibility ellipsoid shape can range from oblate ($T = 1$, $k_1 = k_2 > k_3$) to prolate ($T = -1$, $k_1 > k_2 = k_3$) or present a triaxial neutral fabric ($T \approx 0$, $k_1 > k_2 > k_3$). The AMS lineation is defined as the long axis of the AMS ellipsoid (k_1) and the AMS foliation is the plane bisecting the k_1 and k_2 axes.

To characterize the particles that control the AMS in the Sandfell rhyolite and to test for potential magnetically inverse fabrics, we performed magnetic hysteresis loop measurements and anisotropy of anhysteretic remanence magnetization (AARM) measurements on selected representative specimens. Details of the magnetic characterization and AARM measurements are given in Supp. Mat. 1. All AMS and characterization data collected for this study are provided in Supplementary Material 4.

4. Results

4.1. Structural features observed in the field

We recorded a range of structural features that are spatially and geometrically related to magmatic textures in the Sandfell laccolith; examples of each feature are shown in Fig. 2. The most abundant feature is flow banding, which is characterized by the alignment of the sparse feldspar phenocrysts and alternating changes in the color of the rhyolite between medium grey and beige/tan (Fig. 2a, b). Generally, grey flow bands are dense and hard, while the tan flow bands exhibit a visible vesicularity and are less resistant to weathering. The latter are thus termed porous flow bands. Consequently, flow banding coincides with a platy parting of the rhyolite in outcrop. In some outcrops, the pores in the porous flow bands are elongate perpendicular to the flow band strike and line up in the flow band plane where they form wavy linear arrangements and are here termed 'pore channels' (Fig. 2c, d). The spacing between neighboring flow bands and pore channels is on the order of 1 cm.

The most striking features observed were arrays of sharp fractures arranged with regular spacing within individual flow bands (Fig. 2e-g). The fractures are uniform in height and width, <5 cm tall, and evenly spaced on a millimeter to centimeter scale. These "fracture bands" (Mattsson et al., 2018) can be followed for decimeters to several meters and can end abruptly or pinch out. Fracture bands often follow the flow banding and are surrounded by coherent, unfractured rhyolite of the dense grey type mentioned above. Spacing between fracture bands ranges from the centimeter to meter scale. Quite frequently fracture bands also cut across the flow banding in a wavy fashion and cross over to other flow bands. In several locations, we found larger (>5 cm thick) fracture bands that can also contain more than one set of fractures, i.e. the fractures crosscut each other within the fracture-band plane ('large' fracture bands; Fig. 2h-j). Occasionally, fracture bands overlap so individual fracture sets become indistinguishable, and the rock appears brecciated (Fig. 2k, l). Within this breccia, some planes appear entirely crushed resembling a fault gouge (Fig. 2m). A summary of these observations, along with their outgassing potential (discussed in Section 5.4), can be found in Table 2.

4.2. Results of structural analysis

The results of our structural mapping show are summarized in Figure 3. Flow bands throughout the laccolith often shallowly dip to the WSW, except for the areas shown by plots II and IV (Fig. 3a). There,

Fig. 2. Categories of deformation features preserved in outcrop at the Sandfell laccolith. a) Porous flow bands have higher porosity and tan color compared to fresh grey rhyolite and often erode in platy parting (b); the walking stick in the photo is ~30 cm. c) Pore channels are defined as irregularly undulating planar pores confined to flow bands, and have sub-regular spacing. Cross-section view and (d) plan view, note pores completely avoid dense grey rhyolite (dashed outline) in non-porous flow bands. e–g) 'Small' fracture bands are defined as being <5 cm thick and having single fracture orientations. h–j) 'Large' fracture bands are ≥5 cm thick (h) and/or have more than one fracture orientation (i, j). k, l) Breccia has no discernible fracture bands, but similar fracture orientation, or can resemble gouge (m).

moderate to steep dips in various directions occur, even in the same local area. Fracture bands dip shallowly and parallel to the flow bands near the summits of Upper and Lower Sandfell (plot VII, Fig. 3a). In the northern part of the laccolith, plot II shows fracture bands are sub-vertical and strike parallel to the laccolith margin. To the north and south of Lower Sandfell (plots III and V), fracture bands of several orientations occur in close vicinity to each other. Across the whole laccolith, some of the fracture-band orientations are sub-parallel to the flow banding (plots I, III, V, VI, and VII, Fig. 3a) and some fractures are parallel to flow bands (plots V and VII, Fig. 3a). However, fracture bands are often discordant to flow bands (plots II and IV, Fig. 3a). North of Lower Sandfell (plot III, Fig. 3a), fracture bands generally have shallow *E*ward dips and moderate NE dips, while in the southeast (plot IV, Fig. 3a), fracture bands are either subvertical and N-S striking or shallowly NW-dipping. South of Lower Sandfell (plot V, Fig. 3a), fracture bands dip shallowly to the S, or moderately to the W or ESE. South of Upper Sandfell (plot VI, Fig. 3a), fracture bands dip SW-ward.

The orientations of fractures within fracture bands in the main laccolith body show dominantly E-W strikes with moderate to steep dips towards S or N (plots III-VII, blue poles, Fig. 3a). Near the summit (plot VII), steep N- and EW-dipping fractures occur in the fracture bands, while in the north (plot II), fractures dip moderately to the W. North of Lower Sandfell, (plot III), fractures in fracture bands dip moderately to steeply towards SW.

The angle between the fracture plane and the associated fracture band plane, which was measured using stereographic projection (Supp.

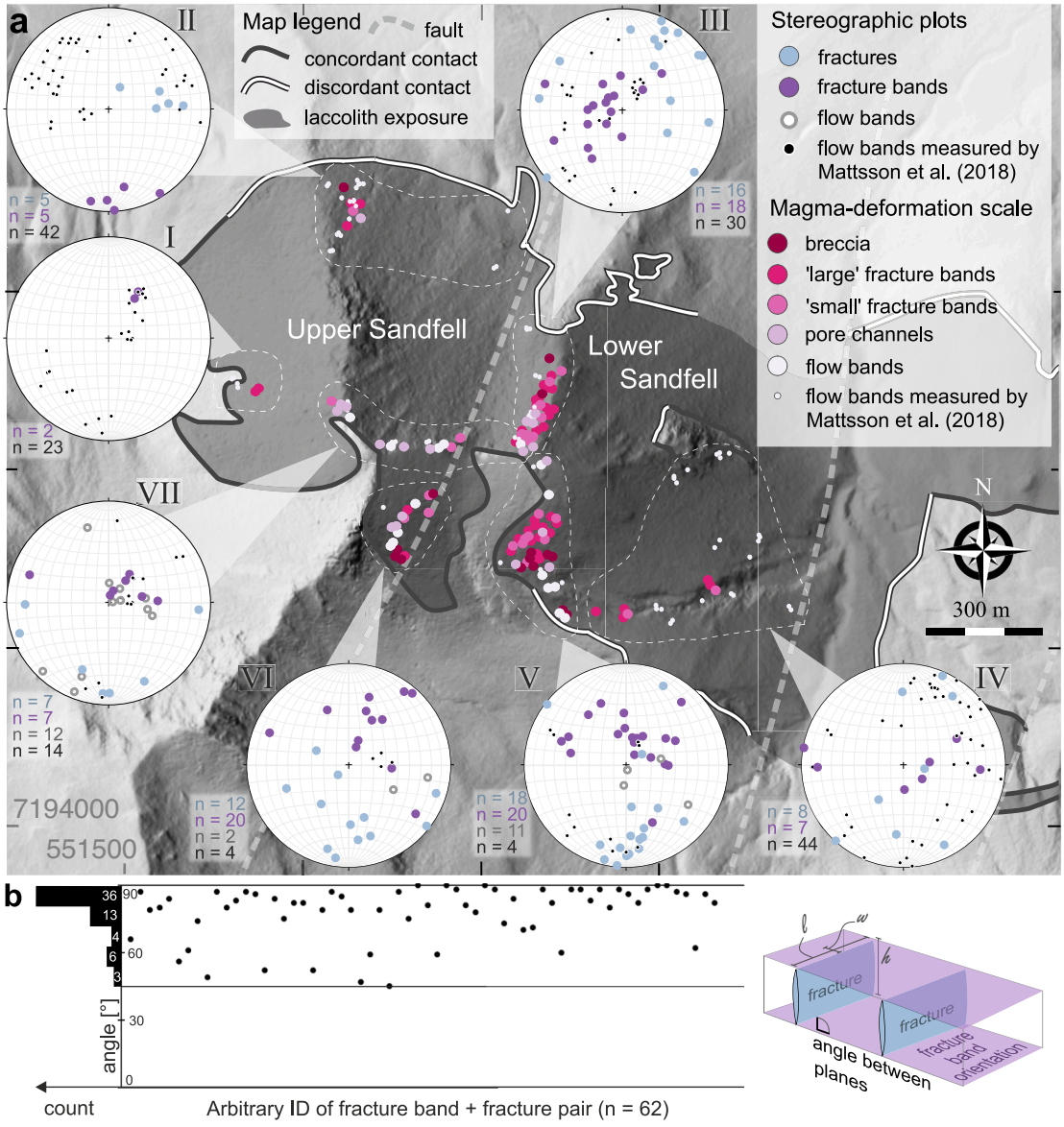

Fig. 3. Structural and deformation map overlain on digital elevation model (DEM) from Landmælingar Íslands. Coordinates are in UTM 28 N. a) Pink dots show a qualitative degree of deformation from outcrop photography. Stereonets show flow band (black) and fracture band (blue/purple) orientations in the regions outlined by dashed lines. b) Measured angle between fracture band and the resident fractures' orientation. Left of y-axis is a histogram of data distribution. The minimum angle between the fracture and fracture band measured is 45° (solid middle line). Schematic drawing of plotted parameters to the right; l = length, w = width, h = height of fracture. (For interpretation of the references to color in this figure legend, the reader is referred to the web version of this article.)

Mat. 2) shows that fractures are dominantly oriented at right angles to their host fracture band (Fig. 3b). In some outcrops, a single fracture band contains a fracture set that abruptly changes orientation, and often neighboring fracture bands contain fractures with dissimilar orientations. In the case where two measurable fracture sets exist within one fracture band, the angle between the fractures ranged from 19 to 107° (Supp. Mat. 2).

4.3. Virtual outcrop analysis

A virtual outcrop model created by UAV photographs reveals distinct flow domains along Transect 1 in the laccolith (Fig. 4). Below the basalt lava roof at Upper Sandfell, we observe a comparatively dark, fine-grained layer of rhyolite. Along Transect 1, this unit of darker rhyolite is about 14 m thick and its bottom contact coincides with a zone of intense platy fracturing. The unit of dark rhyolite extends below the peak of the Upper Sandfell and is faulted (in a ductile manner) together with the capping basalt lava flows (faulted in a brittle manner). Therefore, we interpret the dark rhyolite unit as the initial sill that formed during the incipient intrusion growth. Along Transect 1, below the initial sill, we identify three additional units based on platy parting orientations, representing magma flow partition planes within the rhyolite (cf. Mattsson et al., 2018; Fig. 4). Between 14 and ~ 37 m below the basalt roof the platy parting dips shallowly to the S with a mean plane oriented 093/29 (RHR, strike/dip; n = 18); mean planes were calculated with Fisher statistics using the software Stereonet 11 (Fisher et al., 1993; Allmendinger et al., 2011). Between 37 and 87 m below the roof of Upper Sandfell, in the middle of the transect, we note sub-horizontal flow banding/platy parting with a mean plane of 138/15 (n = 14). Between 87 m and the bottom of the transect at 140 m below the roof, we observe shallowly inclined flow banding/platy parting represented by a mean plane oriented 103/25 (n = 16). Virtual outcrop models without annotations can be found in Fig. S5 in Supplementary Material 1.

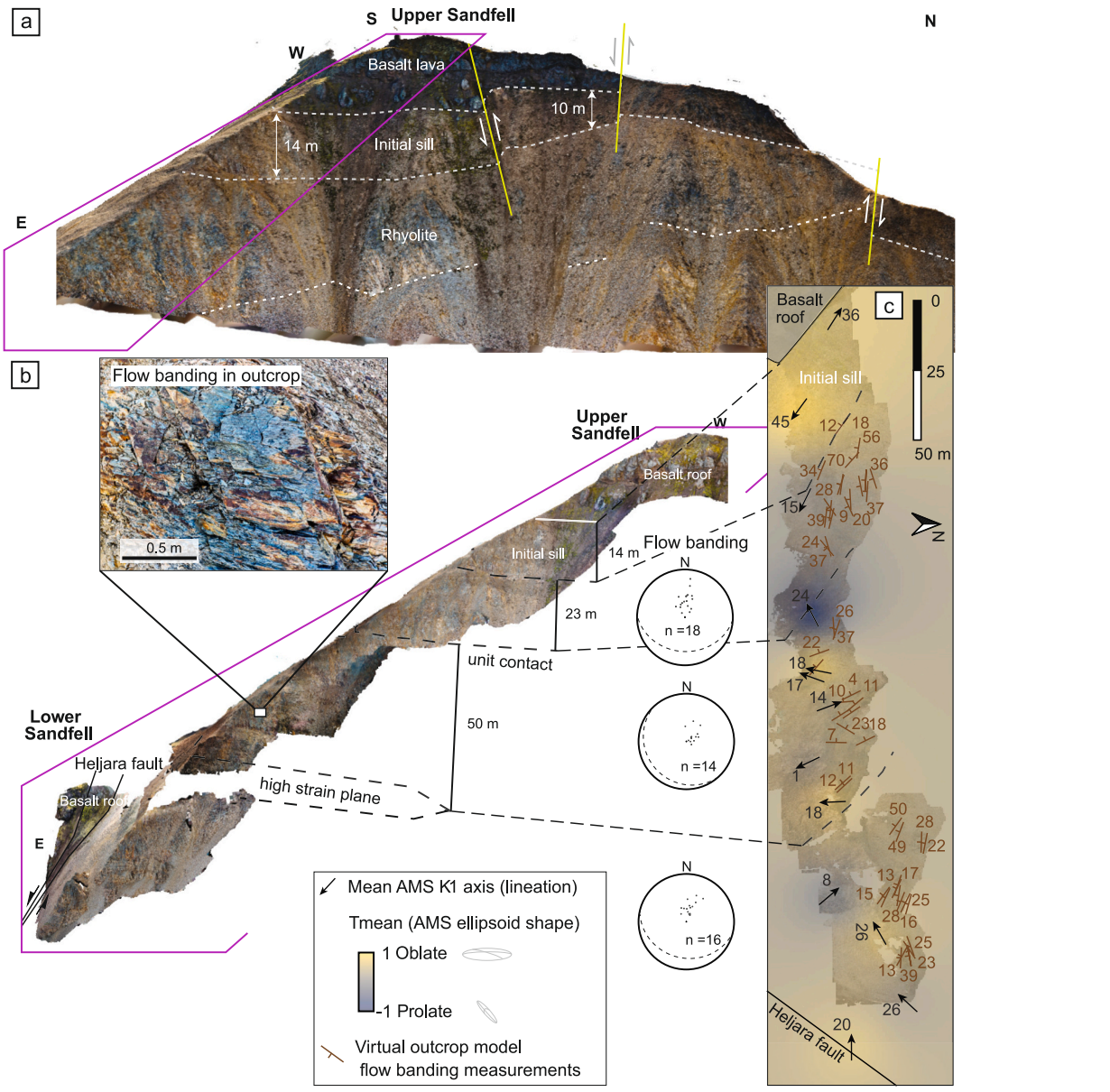

Fig. 4. Virtual outcrop mapping results (outcrop location found in Fig. 5). Flow banding/platy parting measurements and AMS data were used to identify the internal structure along Transect 1 of the Sandfell laccolith. **a & b)** Virtual outcrop models of Transect 1 and the peak of Upper Sandfell. The platy parting was traced on the outcrop models. Stereographic projections of poles to planes on equal area lower hemisphere plots. **c)** Map-view of the virtual outcrop of Transect 1 and orientation markers for flow banding/platy parting in rhyolite. Camera locations and error statistics are shown in Fig. S6.

4.4. AMS

Magnetic characterization experiments and AARM measurements on selected specimens show that the AMS of Sandfell laccolith rhyolite is dominated by multidomain Ti-magnetite grains and that the AARM and AMS fabrics are co-axial (Sup. Mat. 1, Figs. S1 and S2; Mattsson et al., 2018). The AMS fabric is therefore assumed to reflect the magnetite shape petrofabric in the Sandfell rhyolite. AMS data from this study were supplemented with data from Mattsson et al. (2018) to interpret the magmatic strain distribution within the laccolith. Fig. 5 shows a map of AMS lineations and contours of AMS fabric shape in the main body of the Sandfell laccolith.

The mean susceptibility (*Km*) of samples used for interpretation of magma flow within the Sandfell laccolith (n = 63, excluding heavily altered samples of Mattsson et al., 2018) range from 5.62×10^{-4} to 1.54×10^{-2}, with an average of 7.65×10^{-3} (1σ, 3.78×10^{-3}; Fig. S3). The corrected degree of susceptibility (*Pj*) ranges from 1.006 to 1.112 with an average of 1.04 (1σ, 0.02; Fig. S3). AMS lineations (sample site mean ellipsoid K_1 axis) are dominantly shallowly plunging (<33°) in the main body of the Sandfell laccolith. The lineations trend ESE or WNW closest to the roof of the laccolith at Upper and Lower Sandfell and roughly N-S about 40 to 50 m below the roof in transects 1 and 3 (Figs. 5 and S4). AMS lineations at a vertical distance >110 m below the basalt lava roof of Upper and Lower Sandfell along transects 1 and 3 are dominantly shallow to moderately plunging (<33°) and trend SW. In transect 2, the lineations dominantly trend SW with shallow to steep plunges but are truncated by NNW to SSE trending lineations at two sites along the transect (Figs. 5 and S4).

The AMS foliations range from shallow- to steeply-dipping with marked changes in strike in sections along the sampling transects in the main body (Fig. S3). The shape of the AMS fabric is dominantly oblate (T = ~0.85 to 0.3) to transitional oblate (T = 0.3 to 0) close to the roof of Upper and Lower Sandfell. However, the fabrics are dominantly prolate shaped (T = ~ − 0.7) at about 30 to 40 m below the roof in transects 1

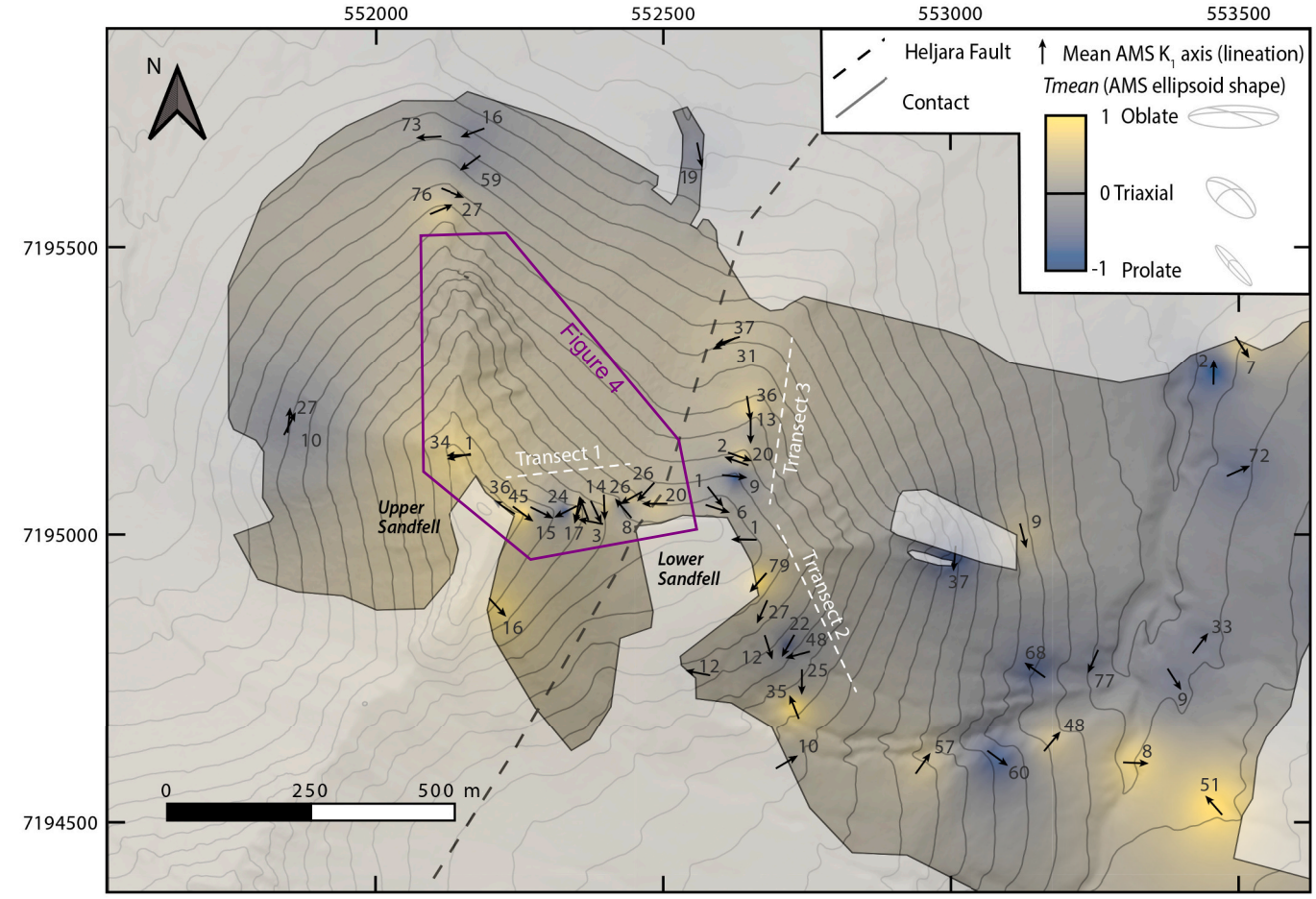

Fig. 5. Map of AMS lineations and contours of AMS fabric shape parameter (*T*) in the main body of the Sandfell laccolith. Data from this study and Mattsson et al. (2018). The AMS fabric shape (T factor) is illustrated on an Inverse-Distance Weighting contour map overlaid on an Arctic DEM of the Sandfell laccolith. All AMS data collected for this study are provided in Supplementary Material 4. DEM created by the Polar Geospatial Center from Maxar Imagery (Porter et al., 2023). Coordinate system UTM 28 N.

and 3 (blue areas in Fig. 5). In transect 2, a zone of dominantly prolate to transitional prolate ($T = 0$ to -0.3) fabrics occurs at around 110 m below the roof of Lower Sandfell. A detailed view of transect 1 is shown in Fig. 4c. Transects 2 and 3 are displayed in detail in Fig. S4.

5. Discussion

According to Mattsson et al. (2018), the fracture bands in the Sandfell laccolith record brittle deformation of the magma concurrent to its emplacement. These authors further proposed that flow bands originated during the early, endogenous sill inflation while fracturing in some of the flow bands occurred during the sill-to-laccolith transition. Finally, Mattsson et al. (2018) qualitatively inferred that fracturing had a profound effect on the degassing of the magma. In this discussion, we explore the hypotheses posed by Mattsson et al. (2018), systematically investigate both brittle and viscous deformation of the Sandfell laccolith magma, and discuss the implications of these processes for magma emplacement dynamics and outgassing.

5.1. Viscous to brittle magma deformation continuum

We observed different types of structural features in the Sandfell rhyolite, ranging from porous flow bands to fracture bands and brecciation (Fig. 2; Table 1). The groundmass and pore geometries found in the flow bands of the Sandfell laccolith are similar to those found in rhyolite lava at Aso volcano (Japan) reported by Furukawa and Uno (2015).

Table 1
Terminology used in the manuscript.

Term	Definition	Location
Oblate AMS fabric	Pancake-shaped ellipsoid	Figs. 4, 5
Prolate AMS fabric	Cigar-shaped ellipsoid	Figs. 4, 5
Mode 1 fracture	Tensile; minimum principal compressive stress σ_3 orthogonal to local plane of crack surface	Section 5.2
Mode 3 fracture	Out-of-plane shear; minimum principal compressive stress σ_3 parallel to both the crack surface and crack front	Section 5.2

Flow bands have been proposed to form primarily due to slight differences in water content (Nelson, 1981; Seaman et al., 2009), which causes viscosity contrasts that result in shear localization and contrasting shear rates. Different applied shear rates have different effects on the magma, localizing stress in wide (low strain rate) or narrow (high strain rate) shear zones that can result in varying microlite abundances (Gonnerman and Manga, 2003) and could lead to higher porosity from preferential volatile exsolution. Another model for flow band formation comes from the viscous annealing of particles within fractures (Tuffen et al., 2003; Tuffen and Dingwell, 2005). While investigating the origins of the flow bands in the Sandfell laccolith was outside the scope of this study, we acknowledge the plausibility of all three mechanisms: varying water content leading to shear-zone localization, concentrations of

microlite growth, and annealing of transient magmatic fractures and clastic veins.

Pore channels are reported in trachydacitic lava by Vezzoli et al. (2023; but referred to as 'vesicle trains'), where it was possible to correlate the long axis of the pores as parallel with the lava flow direction. Vezzoli et al. (2023) interpret their elongate formation as active degassing assisted by shear, which drove bubbles to coalesce in the viscous lava and form channels, bound at the upper and lower limits by what we assume is the original flow band and therefore some viscosity contrast, which inhibited further outward propagation. The appearance of those 'vesicle trains' matches the features found at Sandfell, except at a larger scale. In contrast to the interpretation by Vezzoli et al. (2023), we chose the term 'pore channels' for our intermediate features, because it is not clear that porosity in the porous flow bands of Sandfell is made up of vesicles, which implies the expansion of gas bubbles in the melt (see Witcher et al., *submitted*). Exposures of the plane of pore channels (Fig. 2d, Supp. Mat. 3.2) show linkage of the pores along the flow band plane. Connected pores have a higher permeability than isolated pores, resulting in the pore channels' higher potential for outgassing than regular porous flow bands (Table 2).

Fractures, fracture bands, and breccias in silicic magmas and pyroclasts have been observed in cryptodomes (Burchardt et al., 2019; Galland et al., 2023), lavas (Heiken et al., 1988; Smith et al., 2001; Tuffen and Dingwell, 2005; Smith et al., 2011; Shields et al., 2016; Farquharson et al., 2016; Isom et al., 2023), pyroclasts (Castro et al., 2012; Schipper et al., 2013; Saubin et al., 2016; Wadsworth et al., 2022), and rheomorphic ignimbrites (Andrews and Branney, 2011), and are interpreted to reflect brittle deformation of viscous magma as a result of shear, applied by magma movement or volatile overpressures (Kendrick et al., 2017; Kushnir et al., 2017; Hornby et al., 2019). Degassing and potential outgassing of magma near conduit walls are strongly associated with tuffisite formation (Cabrera et al., 2011; Shields et al., 2016;Heap et al., 2019b; Unwin et al., 2021), but observations of the characteristic pyroclast-filled veins with various degrees of welding on the macro- and micro-scale are few and far between in the Sandfell laccolith (in microscale, see companion paper). Castro et al. (2012) describe the necessity of densely-spaced fractures to effectively degas magma, as there are more surfaces to degas from. They modeled spacings on the order of 0.01–0.001 m, which matches the range of fracture spacing within fracture bands found at the Sandfell laccolith (Fig. 2). The close spacing of fractures, length scales of fractures and fracture bands, and concentric layering of fracture bands point to a very efficient degassing and outgassing mechanism (cf. Crozier et al., 2022). We speculate that this is why there is an absence of tuffisites: volatile pressures were released through fracture banding and subsequent outgassing before they reached the levels required to rupture and fragment the magma to form tuffisites. For these reasons, we rule out tuffisite formation when interpreting the primary mechanisms that formed the brittle features described here.

Table 2
Structural features found in outcrop at the Sandfell laccolith, and their defining characteristics.

Feature name	Defining characteristics	Outgassing potential
Porous flow bands	Tan color, higher porosity than neighboring flow band, platy erosion, visible crystal alignment (Fig. 2a, b)	Lowest
Pore channels	Semi-organized, sub-vertical pores confined to flow bands (Fig. 2c, d)	Low
Fracture bands (small)	Sharp, linear fractures with mm-scale width, cm-scale height, dm- to m-scale lengths; uniformly spaced and organized in a meter-scale band; <5 cm thick and/or 1 fracture set (Fig. 2e-g)	Moderate
Fracture bands (large)	Same appearance as small fracture bands, only larger; ≥5 cm thick (Fig. 2h) and/or > 1 fracture set within the single band (Fig. 2i-j)	Moderately high
Breccia	Indistinguishable bands with similarly oriented fractures (Fig. 2k, l), or complete gouge (Fig. 2m)	High

Although all the features described in this study have been recorded in intrusive and extrusive magmatic settings, the Sandfell laccolith is an exceptional case, in which the entire spectrum of the above-described deformation features is excellently preserved and their interrelationships displayed. The case of Sandfell shows that porous flow bands, pore channels, fracture bands, and breccia (Fig. 2; Table 1) are sequential products of a continuum between viscous and brittle magma deformation. Flow bands and pore channels represent viscous magma flow, while fracture bands and breccias record repeated or continuous strain applied at a higher rate than the magma could accommodate through viscous relaxation (i.e. excursions into the brittle regime). In agreement with Mattsson et al. (2018), we expect that brittle features were preserved partly because the pressure drop caused by fracturing rapidly drew magmatic volatiles into fractures, which froze the immediately surrounding magma by dehydration (Tuffen et al., 2022). However, Witcher et al. (*submitted*) provide evidence that there was a rheological contrast between the now-fractured magma and the over- and underlying microcrystalline magma with a higher crystal fraction. Therefore, brittle deformation was facilitated by mechanically weak layers in the rhyolite close to the solidus temperature, and resulted in dehydration of the residual melt that led to rapid solidification (Witcher et al., *submitted*). In the more viscous scenario, thermal equilibration and viscous relaxation would have deformed the fractures and reduced porosity, perhaps presenting features interpreted as pore channels or porous flow bands in the field. If repeated or continued applied stress outpaced viscous relaxation, small fracture bands grew and the magma was brecciated.

5.2. Outcrop-scale styles of magma deformation

In order to decipher what the distribution and orientation of the observed deformation features reveal about magma emplacement, we conducted structural mapping and analysis.

It is worth noting that the Sandfell laccolith was subject to regional tilting together with the rest of Eastern Iceland long after volcanic activity ceased, (ca. 10–15° W to SW; Óskarsson and Riishuus, 2013; Burchardt et al., 2022). Walker (1974) showed that regional tilt varies with elevation, and it is not precisely known how much tilting individual areas experienced at the scale of our study area. For this reason, we chose not to correct our structural data for the regional tilt, which ultimately allows for comparison to data from other studies, which are also uncorrected. We do, however, distinguish regional tilting from magma-induced deformation at the host rock contacts.

The shallow-dipping flow banding in the Sandfell laccolith, which was originally concordant with the host rock contact, likely reflects lateral magma propagation during sill emplacement. Deviations from the horizontal dips may be explained by the deformation of the early flow banding by later pulses of magma (e.g., plots II and IV, Figs. 3a & 4a). Fracture bands that are discordant to flow bands (plots II, III, Fig. 3a) may be younger and reflect a different stress field than that which formed the flow bands. Since increasing crystal fraction brings magma closer to brittle failure, it is logical to assume the brittle features in outcrop are younger than their viscous counterparts, due to the degree of groundmass crystallization increasing with time.

Fractures are dominantly oriented 90° to their associated fracture band (Fig. 3b). This sets them apart from arrays of Riedel structures, which form ~70° to the shear plane and are not tensile (Ahlgren, 2001). While there is a visible tensile component to the fractures at Sandfell, they are not likely to be purely mode 1, given their extensive lengths (Fig. 6, Supp. Mat. 3). Those lengths, we propose, are caused by shearing of the magma, in mode 3. We therefore settle on a mixed-mode mechanism of fracture formation, with simple shear controlling their lengths in the shear plane (mode 3) and a component of pure shear opening

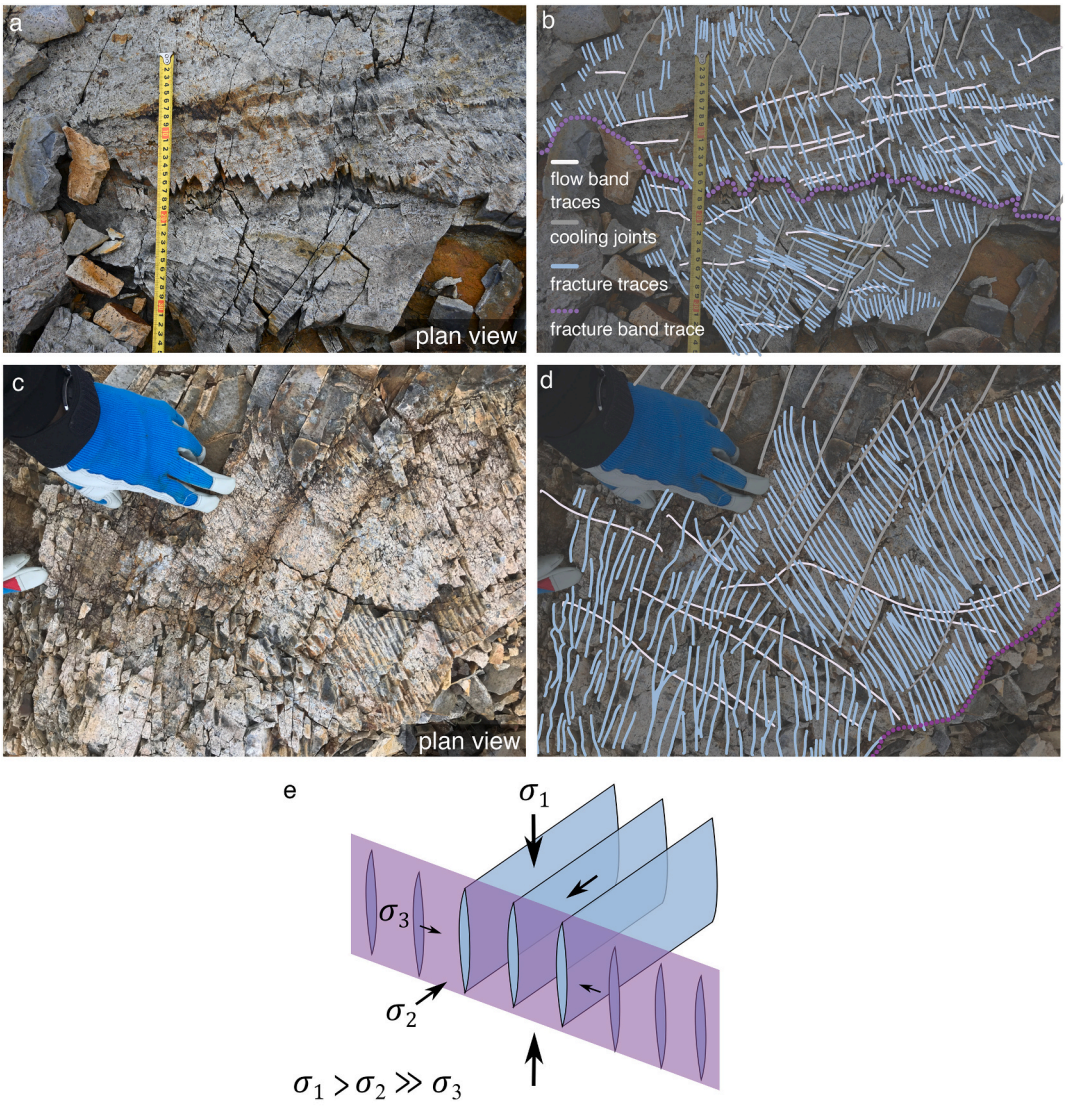

Fig. 6. Plan-view examples of two different fracture sets with outcrop photographs right and interpretations left. **a & b)** Fractures (blue) in two fracture bands, separated by a thin layer of dense unfractured rock (traced in purple). Traces of flow bands (light grey) and cooling joints (dark grey) are highlighted as well. **c & d)** Two fracture sets (blue) within the same band (outlined by purple), along with traces of flow bands and cooling joints. **e)** Schematic drawing of principal compressive stress orientations associated with our model for fracture band formation. (For interpretation of the references to color in this figure legend, the reader is referred to the web version of this article.)

them in tension (mode 1; Table 1; Fig. 6e). The lack of displaced markers within the magma keeps us from definitively knowing the shear motion, but simple shear of intruding magma plus pure shear from compression against the host rock during inflation stand out as two plausible stress environments.

Fracture orientations can change abruptly in fracture bands at decimeter to meter scale (Fig. 6a), even within the same fracture band (Fig. 6b). We measured five cases of fracture bands with two fracture sets (many more we observed, but could not be confidently measured). Of those five, two fracture sets have an acute angle of 55° and 66° relative to each other (considered conjugate). The other three have an acute angle of 19°, 30°, and 73° relative to each other. Therefore, the stress field controlling their formation was either highly spatially variable or temporally variable to facilitate the formation of multiple fracture sets. Nevertheless, large fracture bands most often record multiple (>2) shear directions (Fig. 2i, j), the relative ages of which cannot be distinguished. Therefore, the stress field was indeed shifting during the various stages of fracture band growth. This argument is further supported by the alternating AMS fabric orientation and shape and flow banding/platy parting, which show sudden changes in fabric attitude, which we relate to changes in the laccolith growth direction and mode as pulses of magma intruded (Figs. 4 & 5).

Because of the mixed-mode fracture mechanism and the rapid spatial changes in fracture and fracture band orientations, we cannot reconstruct the local stress fields that formed them. As illustrated by the flow band orientations, it is not possible to identify how much these structures have been rotated since their formation. The stress environment of an inflating laccolith is dynamic, constantly changing in space and time, and is also highly variable at different scales (e.g., Burchardt et al., 2019). Also worth considering is the possibility of laccolith deflation post-emplacement as a process leading to fracture formation, as recorded during the Cordón Caulle eruption (Castro et al., 2016). While we cannot determine the exact timing of magma deformation, we favor the brittle deformation taking place during inflation due to the microcrystalline texture of the groundmass driving the magma towards rapid rheological lock-up. We envisage the high crystal fraction preventing significant volume decrease post-emplacement. Additionally, our data show that the orientation of fracture bands almost always overlaps with

the flow band orientations. We interpret these data to mark a transition from viscous to brittle deformation of the magma, which likely took place during laccolith growth.

Shear stresses responsible for flow banding and cavitation (pore channels) eventually drove the magma to fracture as the stress field fluctuated, concomitant to rheology evolution through increasing crystallinity, cooling, and degassing. In cases where fracture bands are concordant to flow bands, the onset of brittle deformation could have been caused by an increase of bulk viscosity from microlite crystallization or an increase in applied shear rate (Tuffen and Castro, 2009; see

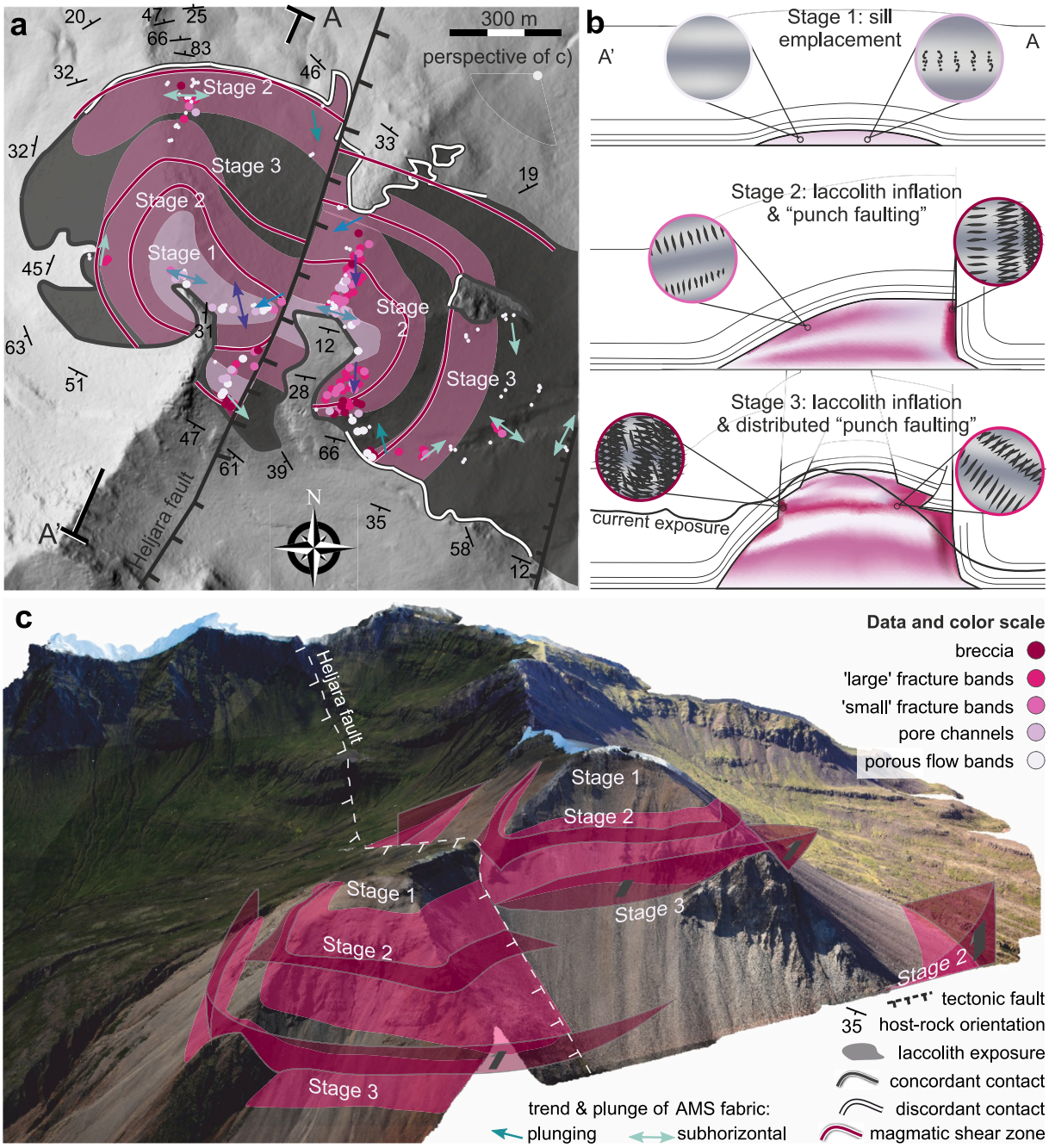

Fig. 7. Conceptual model of the growth of the Sandfell laccolith, based on interpreted field data, AMS fabrics, and deformation features in the rhyolite. **a)** Map view of the main body of the Sandfell laccolith, with observed degree of deformation (pink dots) and AMS trends (arrows). Pink regions highlight areas of high strain, and pale regions highlight areas of lower strain. Circumferential shear zones (dark pink lines) represent magmatic shear zones resulting in 'punch' faulting of the inflating laccolith. The laterally continuous units with distinct flow fabrics in the main body of the laccolith suggest that the Sandfell laccolith grew in pulses with the highest strain recorded at the interface between units of magma. However, the time scale between pulses in the Sandfell laccolith cannot be established, but extrusive volcanic domes which show short intermittent growth pulses during dome-building events spanning decades (Ogburn et al., 2015). Host rock attitudes from Twomey (2023), DEM courtesy Landmælingar Íslands. **b)** Schematic drawing of cross section A-A': Stage 1: dominantly viscous deformation (porous flow bands and pore channels depicted) during the emplacement of the initial sill; Stage 2: steeply inclined fracture bands develop on the north margin, accommodating high strain rates and crossing the brittle transition (small and large fracture bands depicted). Stage 3: Continued punching: brittle regime dominates as deformation mechanism, strain localizes along weakened zones in the rhyolite and continues to fracture, circumferentially propagating punch faults. (c) Virtual outcrop of the Sandfell laccolith main body produced from oblique aerial photographs, overlain with high shear zones from a) and b). Normal faulting offset caused by tectonic Heljara fault post emplacement. (For interpretation of the references to color in this figure legend, the reader is referred to the web version of this article.)

also Witcher et al., *submitted*). In cases where fracture bands are discordant to flow bands, the local stress field must have shifted, and localized shear along a different plane. The resulting structures were locked into the strain archive near the end of the magmatic life of the laccolith. Hence, the distribution and orientation of these deformation features are evidence of the relationship between magma emplacement and deformation.

5.3. Laccolith-scale strain partitioning

Fig. 7 presents a new conceptual laccolith inflation model for the Sandfell laccolith based on our combined field-based deformation map (pink points), virtual outcrop mapping, and AMS fabric data (arrows). Areas with high degrees of brittle deformation, in the Sandfell laccolith (Fig. 3), together with the abrupt shift in AMS and flow band orientations (Figs. 3 & 4), are used to delineate structural units in the rhyolite that are interpreted here in the context of laccolith emplacement (shaded pink areas, Fig. 7). Using virtual outcrops, we extrapolated our observations to inaccessible areas and identified matching structural domains on either side of the Heljara fault. Our mapping of the distribution of magmatic structures (Fig. 3a) shows that the summit of Upper Sandfell represents a low-strain area. The dominantly viscous deformation features (porous flow bands and pore channels) and oblate magnetic fabrics are parallel to the dominantly concordant roof contact (Figs. 1c and 7a). We infer that this part of the Sandfell laccolith likely records early emplacement of a sill, i.e., dominantly lateral propagation of magma (Fig. 7b), with the AMS fabrics indicating ESE-WNW-directed stretching, corresponding to magma flow. In the virtual outcrops, we were able to measure the thickness of the top (initial) sill at the peaks of Lower and Upper Sandfell to ~14 m (Fig. 4).

The average AMS lineations of the sample sites below the initial sill domain are sub-horizontal, trending NNW-SSE highlighting a shift to NNW-SSE stretching linked to the propagation of magma to the NNW (Fig. 4). By combing AMS and virtual outcrop measurements of flow banding/platy parting we note at least three (stacked) sill-shaped units with a cumulated thickness of about 90 m at Transect 1 along the Heljara fault scarp between Upper and Lower Sandfell (Fig. 4). The occurrences of breccia south and north of Lower Sandfell led us to identify a sub-horizontal shear zone concordant to the flow banding at the bottom of the sill units (marked Stage 2–3 in Fig. 7a and c). The same shear zone is seen in the cliff below Upper Sandfell (Fig. 4a). Below this shear zone, a shift in the AMS fabrics to SW-trending lineations and SSW-dipping flow partition planes (Fig. 7a) indicates a change in laccolith growth direction to up to the NE (from Stage 1 to Stage 2; Fig. 7b). Along its northern margin, the Sandfell laccolith is in subvertical contact with steeply dipping host rock tuffs and lavas (Fig. 7a; ~80°; Hawkes and Hawkes, 1933; Twomey, 2023). The high-strain features (large fracture bands and breccia) together with AMS fabrics that indicate a moderate to steeply inclined stretching sub-parallel to the faulted northern margin (Figs. 5 and 7a) show that magma propagation was accommodated by uplift along several sub-vertical faults, giving the laccolith a trap-door punched geometry (Stage 2; Fig. 7b; cf. Hawkes and Hawkes, 1933; Corry, 1988).

Along the northern and southern flank of Lower Sandfell, abrupt changes from shallow- to steeply-plunging AMS lineations coincide with alternating areas of high (large fracture bands and breccia) and low strain (porous flow bands and pore channels) (Figs. 4, 5, 7a, and S4). Notably, the orientation of the AMS lineations (Transects 2 and 3) from the flanks of Lower Sandfell can be correlated to the lineations along the Heljara fault scarp (Transect 1; Fig. 4). The orientation of fracture bands and fractures on the flanks of Lower Sandfell show abrupt changes in the stress field (Fig. 3), which we interpret to reflect the shift in the dominant direction of laccolith growth as the major northwestern punch fault propagated along the northern margin around the main body of the laccolith to the SE.

We identified areas of highest strain (breccia) that line up around the laccolith (Fig. 3). In the virtual outcrops, these areas can be correlated with a shallow- to moderately-dipping ramp thrust in the cliff below Upper Sandfell (Fig. 7c; Stage 3). The same shear zone manifests as a discordant contact with the host rock N and E of Lower Sandfell (Fig. 4), and highly brecciated outcrops South of Lower and Upper Sandfell. There, we interpret the shear zone to be steeply- to moderately dipping away from the center of the laccolith (i.e. normal faulting), based on the orientation of fracture bands (Fig. 3). The host rock at the contact along the flanks is mostly concordant, but abrupt changes in the host-rock dip and locally discordant contacts (Fig. 7a) also point to strain partitioning along the laccolith flanks. Hence, the fault developing in Stage 3 represents a propagating punch fault that accommodated vertical growth of the laccolith.

In summary, contrasting high- and low-strain areas on the laccolith scale would have accommodated both pure shear applied from the vertical component of laccolith inflation, plus simple shear from magma flow-induced doming influenced by the punch fault propagation (Fig. 7b). Brecciation in the rhyolite adjacent to coherent basaltic host rock (e.g. along the N contact) shows that brittle magma deformation occurred prior to host rock failure. Consequently, the location and style of host rock failure was most likely controlled by the location of shear zones/punch faults within the laccolith. Hence, the Sandfell laccolith is an example of magmatic deformation preceding and controlling host rock deformation to dictate emplacement.

Below we summarize the different stages of growth of the Sandfell laccolith in the light of the above established internal structure.

i. Minor to moderately strained magma occurs within the units and is characterized by *small fracture bands* (Fig. 7b, Stage 1; Fig. 2e–g), evenly spaced and with a single orientation aligned with the stress field. Fracturing drew in volatiles and quenched magma in the immediate vicinity (<1 mm) of the fracture (Mattsson et al., 2018). If viscous relaxation took place, the volatiles would be resorbed into the melt.
ii. As emplacement progressed, shear stresses widened existing fracture bands and localized along zones delineating rhyolite unit interfaces that accommodated the lateral propagation/expansion of the laccolith. Fracture bands grew by incremental fracture propagation until they joined an over- or underlying band, or overprinted new fracture sets onto the initial one, resulting in both types of *large fracture bands* (>1 fracture set and > 5 cm thick; Fig. 7b, Stage 2; Fig. 2h).
iii. The highest shear stresses within the laccolith are associated with areas related to the punch geometry of the laccolith, which produced discordant brittle magma deformation relative to the sub-horizontal units in structurally weak, previously-fractured areas, causing strain partitioning between low-strain areas and areas with intense deformation (*large fracture bands* and *breccias*; Fig. 7b, Stages 2 and 3; Fig. 2i–m). The intensely deformed areas inside the laccolith accommodated further laccolith inflation, which we interpret as additional punch faults, resulting in a 'tiered wedding cake' geometry of the main body of the laccolith (Fig. 7b, c).

Hence, the viscous to brittle magma deformation and associated strain partitioning had a profound effect on the emplacement and development of the Sandfell laccolith. This conclusion agrees with recent case studies that highlight the significance of magma rheology on magma emplacement in the shallow crust (Mattsson et al., 2018; Burchardt et al., 2019; Schmiedel et al., 2021), but contradicts the conclusions of analog modelling and field studies that point to the host rocks' rheology as the main control on laccolith emplacement (Schmiedel et al., 2017, 2019; Galland et al., 2022). The northern punched margin and ~ 80° host rock orientation implies a rather steep surface slope in the time following the Sandfell laccolith's emplacement (cf., Schmiedel et al., 2017, 2019). Such steep slopes developing in a

short timescale add to the hazards posed by rapid laccolith growth, including flank collapse driven by over-steepening which could result in an event similar to the 1980 eruption of Mt. St Helens (USA) (Moore and Rice, 1984).

5.4. Implications for outgassing and explosivity potential

Permeability within a magma body allows exsolved volatiles to escape the system by outgassing. Consequently, internal pore pressures may remain beneath critical values that may otherwise lead to fragmentation and explosion (Richard et al., 2013). In the case of the Sandfell laccolith, the absence of silicic eruptive deposits at the palaeosurface, as well as the lack of vent structures (evident from the presence of e.g. tuffisites, strong vesiculation (frothing), marginal brecciation/agglomerates) within the laccolith, demonstrate that Sandfell did not erupt (Giordano et al., 2024). Instead, we argue that the viscous and brittle magma deformation features described here had a profound effect on magma degassing and volatile transport, preventing an eruption. Mineralization types and textures inside the fractures in the fracture bands is further evidence for outgassing, described in the companion paper (Witcher et al., *submitted*).

Based on the data presented in this study, we propose that the degassing and outgassing network within the Sandfell laccolith developed sequentially in response to changes in strain partitioning that facilitated magma flow during different stages of laccolith growth:

1. Early shear partitioning within the magma localized volatile exsolution along melt-rich flow bands, when the bulk crystal content reached ≥45% (see also Witcher et al., *submitted*). Pores grew and merged under shear, effectively dehydrating the melt and thus decreasing its liquidus temperature (Caricchi et al., 2011).
2. Continuous shear along the porous flow bands caused pores to merge and align into elongated planar pore channels, likely via ductile tearing (cavitation). The porosity caused by the pore channels created a mechanical weakness in the magma. Hence, the tips of each pore channel localized stress from the internal pore pressure plus external inflation-related shearing.
3. Finally, the tensile strength of the magma was overcome either through strain imposed on timescales shorter than the relaxation time of the melt, or through the development of force chains in the microcrystalline groundmass, causing brittle fracturing.
4. Upon brittle deformation, outgassing was controlled by fracture opening and growth. Small fracture bands were likely isolated from each other, hindering volatiles from escaping the laccolith. Second boiling events may have contributed to the internal pressurization of the magma (Magnall et al., 2018).
5. Once existing fracture bands grew larger, joined together, and especially when developed into breccia, a permeable fracture network formed within the magma. This network would have been exploited by exsolved magmatic volatiles, which could efficiently travel through the bulk of the magma body, either to reach the host rock and disperse or remain at stable pressures in the fracture bands of the Sandfell rhyolite.

Hence, viscous degassing and cavitation created a mechanical weakness in the magma, which localized brittle deformation and led to outgassing. The extensive fracture network provided an efficient pressure release mechanism that ultimately contributed to the Sandfell laccolith not explosively erupting. Other factors that likely influenced the eruptive potential of the Sandfell laccolith were its initial volatile content, the rate of magma ascent and intrusion, and the rate of deformation-driven degassing and outgassing. Given the low phenocryst content and lack of evidence for hydrothermal alteration, which would be expected in the form of intense mineralization, we estimate the Sandfell rhyolite to have had relatively low water content (<2 wt%).

Volatile exsolution can impart significant stresses on magma, from depressurization (first boiling) and also chemical saturation driven by crystallization (second boiling Tait et al., 1989; Cassidy et al., 2018). The microcrystalline texture of the Sandfell rhyolite may have caused a second boiling event that resulted in porosity development in the more melt-rich porous flow bands, which would have initiated the fracture banding process by locally weakening the magma. Low water contents (1.77 wt%) have been found in the Krafla rhyolite (Zierenberg et al., 2013) in Northern Iceland, which resembles the Sandfell laccolith in terms of magma composition, volume, geological setting, and shallow depth. Using the Krafla water content as a proxy for the Sandfell rhyolite, we show that a range of pressures representing depths of 700—400 m intersects with solubility curves for water contents between 1.5—2 wt % (Liu et al., 2005) at realistic temperatures for near-solidus rhyolite magma (700—500 °C; Fig. 8). Felsic magmas at H_2O saturation conditions are at a higher risk of explosive eruption, as shown by multiple H_2O contents modeled by Brookfield et al. (2023). This shows that, even at low water contents, the Sandfell laccolith efficiently outgassed and avoided overpressurization.

The low water content of the Sandfell laccolith rhyolite may have allowed for the outgassing system to remain open for timescales sufficient to release pressure, due to the higher melt viscosity having a longer relaxation time. The longer relaxation times would have aided in the preservation of the deformation features observed in outcrop. The low water content may have also prevented widespread hydrothermal alteration, which can drastically reduce porosity and permeability in magmatic systems, leading to overpressurization and explosion, through the sealing pores and fractures (Heap et al., 2019a). The low volatile content might also explain why similar deformation and outgassing features have not been reported more frequently from other magmatic settings where hydrous fluids overprint primary textures. However, the lack of more observations may also be due to reporting bias, as more and more examples of such features are identified from the scientific literature, for instance in two trachyandesitic cryptodomes (Burchardt et al., 2019; Galland et al., 2023), lava domes in Japan (Smith et al., 2001), a deep hydrous granite pluton (Riley and Tikoff, 2010), and dacitic lava (Vezzoli et al., 2023). We show here that deformation-induced outgassing mechanisms are prevalent in the sub-volcanic upper-crustal intrusive environment, including locations other than the volcanic conduit.

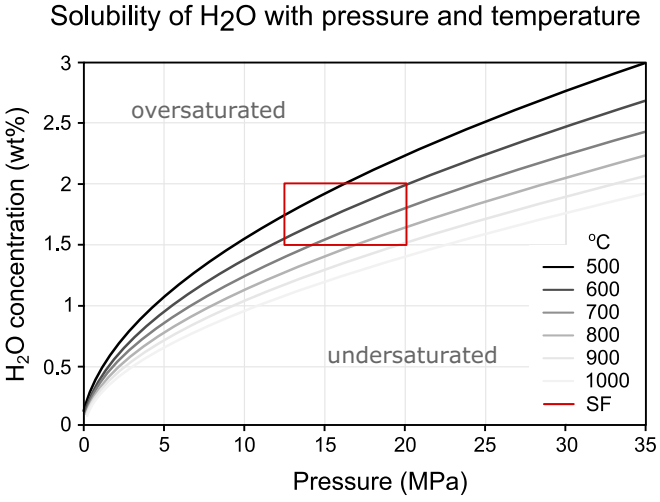

Fig. 8. Solubility curves for water in rhyolitic melt at different pressures and temperatures (Liu et al., 2005). The red box denotes the likely range of conditions in the Sandfell rhyolite (SF) during laccolith inflation, using the Krafla rhyolite water content of 1.77 wt% (Zierenberg et al., 2013) as a proxy. This model does not include CO_2 content. See text for further explanation. (For interpretation of the references to color in this figure legend, the reader is referred to the web version of this article.)

6. Conclusions

The Sandfell laccolith hosts an entire spectrum of related viscous-to-brittle magma deformation features, which likely accommodated magma degassing, and eventually outgassing through fracturing. During the sill-to-laccolith stage, viscous *flow bands* with higher vesicularity (porous flow bands; Fig. 2a, b) evolved into bands of vertical planar pores with continued applied shear, termed here *pore channels* (Fig. 2c, d). Those planar pore channels coalesced while filling with exsolved volatiles, and eventually nucleated fracture propagation when pore pressure plus inflation stresses exceeded the tensile strength of the magma (rock equivalent: *small fracture bands,* Fig. 2e-g). Continued propagation localized magma flow and increased band thickness (rock equivalent: *large fracture bands,* Fig. 2h). Upon further laccolith inflation, shear stresses reactivated existing fracture bands in different directions, overprinting original fracture sets (rock equivalent: *large fracture bands,* Fig. 2i, j). Brittle deformation continued to repeatedly fracture areas of intense strain localization related to circumferential punch faulting of the laccolith margins, resulting in brecciation (Fig. 2k-m). By this account, we argue that brecciated areas reflect the highest stress localized within the magma in underdeveloped punched margins during laccolith inflation, and that magma deformation preceded the overlying host rock failure.

We argue that the Sandfell laccolith effectively released its internal volatile pressures through the permeable fracture network that was developed by the processes described in this study. Brecciated areas would have been the most efficient outgassing pathways, demonstrating that intrusion growth produces magma outgassing pathways. Based on our conceptual model, the Sandfell laccolith flanks would have rapidly grown quite steep, which comes with its own set of hazards to the immediate surroundings (e.g., flank collapse). However, no evidence of an eruption or other catastrophic event is found associated with the Sandfell laccolith. Given their occurrence in other magmatic settings, we propose that the fracture banding mechanism should be considered in all silicic/high-viscosity magma bodies, as an example of viscous and brittle deformation processes working in tandem to degas and outgas magma.

Funding information

TW was funded by a Knut and Alice Wallenberg fellowship to SB (KAW2017–0153). TM was funded by the Swedish Research Council grant (2019–06300). MJH acknowledges support from the Institut Universitaire de France (IUF).

CRediT authorship contribution statement

Taylor Witcher: Writing – review & editing, Writing – original draft, Methodology, Investigation, Formal analysis, Data curation, Conceptualization. **Steffi Burchardt:** Writing – review & editing, Visualization, Supervision, Project administration, Investigation, Funding acquisition, Formal analysis, Data curation, Conceptualization. **Tobias Mattsson:** Writing – review & editing, Visualization, Methodology, Investigation, Formal analysis, Data curation. **Michael J. Heap:** Writing – review & editing, Supervision. **William McCarthy:** Writing – review & editing, Resources, Methodology.

Declaration of competing interest

The authors declare that they have no known competing financial interests or personal relationships that could have appeared to influence the work reported in this paper.

Data availability

All data is included in the supplementary materials.

Acknowledgements

We thank Rafael Horota for the photosphere images and Birgir Oskársson for aerial photographs. We are grateful for constructive and helpful revision comments from Hugh Tuffen and an anonymous reviewer. We also acknowledge editor Ed Llewellin for the solubility curve data and fruitful discussion. We thank Orlando Quintela, Sonja Greiner, Emma Rhodes, and the Liverpool Magma Lab Group for field assistance in 2021. We thank members of the "Magic Mystery Tour" 2019 for insightful discussions in the field. *DEM provided by the Polar Geospatial Center under NSF-OPP awards 1043681, 1559691, 1542736, 1810976, and 2129685.*

Appendix A. Supplementary data

Supplementary data to this article can be found online at https://doi.org/10.1016/j.jvolgeores.2024.108166.

References

Ahlgren, S.G., 2001. The nucleation and evolution of Riedel shear zones as deformation bands in porous sandstone. J. Struct. Geol. 23, 1203–1214.
Alidibirov, M., Dingwell, D.B., 1996. Magma fragmentation by rapid decompression. Nature 380, 146–148.
Allmendinger, R.W., Cardozo, N., Fisher, D.M., 2011. Structural Geology Algorithms: Vectors and Tensors.
Andrews, G.D.M., Branney, M.J., 2011. Emplacement and rheomorphic deformation of a large, lava-like rhyolitic ignimbrite: Grey's Landing, southern Idaho. Bull. Geol. Soc. Am. 123 (3–4), 725–743. https://doi.org/10.1130/B30167.1.
Borradaile, G.J., Jackson, M., 2010. Structural geology, petrofabrics and magnetic fabrics (AMS, AARM, AIRM). J. Struct. Geol. 32 (10), 1519–1551. https://doi.org/10.1016/j.jsg.2009.09.006.
Brookfield, A., Cassidy, M., Weber, G., Popa, R.G., Bachmann, O., Stock, M.J., 2023. Magmatic volatile content and the overpressure 'sweet spot': Implications for volcanic eruption triggering and style. J. Volcanol. Geotherm. Res. 444 https://doi.org/10.1016/j.jvolgeores.2023.107916.
Burchardt, S., Mattsson, T., Palma, J.O., Galland, O., Almqvist, B., Mair, K., Jerram, D.A., Hammer, Ø., Sun, Y., 2019. Progressive growth of the Cerro Bayo Cryptodome, Chachahuén Volcano, Argentina—Implications for Viscous Magma Emplacement. J. Geophys. Res. Solid Earth. https://doi.org/10.1029/2019jb017543.
Burchardt, S., Óskarsson, V., Gustafsson, L.E., Berg, S.E., Riishuus, M.S., 2022. Geology of a Neogene caldera cluster in the Borgarfjörður eystri-Loðmundarfjörður area. Eastern Iceland. Volcanica 5 (1), 133–161. https://doi.org/10.30909/vol.05.01.133161.
Burgisser, A., Gardner, J.E., 2004. Experimental constraints on degassing and permeability in volcanic conduit flow. Bull. Volcanol. 67 (1), 42–56. https://doi.org/10.1007/S00445-004-0359-5.
Cabrera, A., Weinberg, R.F., Wright, H.M.N., Zlotnik, S., Cas, R.A.F., 2011. Melt fracturing and healing: a mechanism for degassing and origin of silicic obsidian. Geology 39 (1), 67–70. https://doi.org/10.1130/G31355.1.
Caricchi, L., Pommier, A., Pistone, M., Castro, J., Burgisser, A., Perugini, D., 2011. Strain-induced magma degassing: Insights from simple-shear experiments on bubble bearing melts. Bull. Volcanol. 73 (9), 1245–1257. https://doi.org/10.1007/s00445-011-0471-2.
Cashman, K.V., Scheu, B., 2015. Magmatic Fragmentation. In: The Encyclopedia of Volcanoes, 2nd ed. Elsevier, pp. 459–471. https://doi.org/10.1016/B978-0-12-385938-9.00025-0.
Cassidy, M., Manga, M., Cashman, K., Bachmann, O., 2018. Controls on explosive-effusive volcanic eruption styles. Nat. Commun. 9 (2839) https://doi.org/10.1038/s41467-018-05293-3.
Castro, J.M., Cordonnier, B., Tuffen, H., Tobin, M.J., Puskar, L., Martin, M.C., Bechtel, H. A., 2012. The role of melt-fracture degassing in defusing explosive rhyolite eruptions at volcán Chaitén. Earth Planet. Sci. Lett. 333–334, 63–69. https://doi.org/10.1016/j.epsl.2012.04.024.
Castro, J.M., Cordonnier, B., Schipper, C.I., Tuffen, H., Baumann, T.S., Feisel, Y., 2016. Rapid laccolith intrusion driven by explosive volcanic eruption. Nat. Commun. 7 https://doi.org/10.1038/ncomms13585.
Clocchiatti, R., Del Moro, A., Gioncada, A., Joron, J.L., Mosbah, M., Pinarelli, L., Sbrana, A., 1994. Assessment of a shallow magmatic system: the 1888-90 eruption. Vulcano Island, Italy 56, 4–66.
Cordonnier, B., Caricchi, L., Pistone, M., Castro, J., Hess, K.U., Gottschaller, S., Manga, M., Dingwell, D.B., Burlini, L., 2012. The viscous-brittle transition of crystal-bearing silicic melt: Direct observation of magma rupture and healing. Geology 40 (7), 611–614. https://doi.org/10.1130/G3914.1.
Corry, C.E., 1988. Laccoliths: Mechanics of Emplacement and Growth, vol. 220. Geological Society of America.
Crozier, J., Tramontano, S., Forte, P., Jaye, S., Oliva, C., Gonnermann, H.M., Lev, E., Manga, M., Myers, M., Rader, E., Ruprecht, P., Tuffen, H., Paisley, R., Houghton, B. F., Shea, T., Schipper, C.I., Castro, J.M., 2022. Outgassing through magmatic

fractures enables effusive eruption of silicic magma. J. Volcanol. Geotherm. Res. 430, 107617 https://doi.org/10.1016/j.jvolgeores.2022.107617.
Dingwell, D.B., 1996. Volcanic dilemma: Flow or blow?. In: Science, 273. American Association for the Advancement of Science, pp. 1054–1055. https://doi.org/10.1126/science.273.5278.1054. Issue 5278.
Dingwell, D.B., Webb, S.L., 1989. Structural Relaxation in Silicate Melts and Non-Newtonian Melt Rheology in Geologic Processes. In Phys Chem Minerals 16.
Dürig, T., Zimanowski, B., 2012. "Breaking news" on the formation of volcanic ash: Fracture dynamics in silicate glass. Earth Planet. Sci. Lett. 335–336, 1–8. https://doi.org/10.1016/j.epsl.2012.05.001.
Farquharson, J.I., Heap, M.J., Lavallée, Y., Varley, N.R., Baud, P., 2016. Evidence for the development of permeability anisotropy in lava domes and volcanic conduits. J. Volcanol. Geotherm. Res. https://doi.org/10.1016/j.jvolgeores.2016.05.007.
Fisher, N.I., Lewis, T., Embleton, B.J.J., 1993. Statistical Analysis of Spherical Data. Cambridge University Press, Cambridge, p. 343.
Furukawa, K., Uno, K., 2015. Origin and deformation of high porosity bands in the Takanoobane Rhyolite lava of Aso volcano, Japan. J. Volcanol. Geotherm. Res. 305, 76–83. https://doi.org/10.1016/j.jvolgeores.2015.09.021.
Gaillot, P., de Saint-Blanquat, M., Bouchez, J.L., 2006. Effects of magnetic interactions in anisotropy of magnetic susceptibility: Models, experiments and implications for igneous rock fabrics quantification. Tectonophysics 418 (1–2 SPEC. ISS), 3–19. https://doi.org/10.1016/j.tecto.2005.12.010.
Galland, O., de la Cal, H., Mescua, J., & Rabbel, O. (2022). 3-dimensional trapdoor structure of laccolith-induced doming and implications for laccolith emplacement, Pampa Amarilla, Mendoza Province, Argentina. *Tectonophysics*, 836. doi:https://doi.org/10.1016/j.tecto.2022.229418.
Galland, O., Villar, H.J., Mescua, J., Jerram, D.A., Midtkandal, I., Palma, J.O., Planke, S., Zanella, A., 2023. The Long-Term Legacy of Subvolcanic Intrusions on Fluid Migration in Sedimentary Basins: The Cerro Alquitrán Case Study, Northern Neuquén Basin. Basin Research, Argentina. https://doi.org/10.1111/bre.12782.
Gardner, J.E., Llewellin, E.W., Watkins, J.M., Befus, K.S., 2017. Formation of obsidian pyroclasts by sintering of ash particles in the volcanic conduit. Earth Planet. Sci. Lett. 459, 252–263. https://doi.org/10.1016/j.epsl.2016.11.037.
Giachetti, T., Trafton, K. R., Wiejaczka, J., Gardner, J. E., Watkins, J. M., Shea, T., & Wright, H. M. N. (2021). The products of primary magma fragmentation finally revealed by pumice agglomerates. *Geological Society of America | GEOLOGY, 49*. doi: https://doi.org/10.1130/G48902.1.
Gibson, I.L., 1963. The Reydarfjordur Acid Volcano Centre of Eastern Iceland. University of London.
Gibson, I.L., Kinsman, D.J.J., Walker, G.P.L., 1966. Geology of the Fáskrúðsdsfjörður Area. Eastern Iceland, Visindafélag Íslandinga.
Giordano, D., Romano, C., Dingwell, D.B., Poe, B., Behrens, H., 2004a. The combined effects of water and fluorine on the viscosity of silicic magmas. Geochim. Cosmochim. Acta 68 (24), 5159–5168. https://doi.org/10.1016/j.gca.2004.08.012.
Giordano, D., Romano, C., Papale, P., Dingwell, D.B., 2004b. The viscosity of trachytes, and comparison with basalts, phonolites, and rhyolites. Chem. Geol. 213 (1–3), 49–61. https://doi.org/10.1016/j.chemgeo.2004.08.032.
Gonnerman, H.M., Manga, M., 2003. Explosive volcanism may not be an inevitable consequence of magma fragmentation. Nature 426. https://doi.org/10.1038/nature02159.
Gonnermann, H.M., Manga, M., 2009. Dynamics of magma ascent in the volcanic conduit. In: Modeling Volcanic Processes: The Physics and Mathematics of Volcanism. Cambridge University Press, pp. 55–84. https://doi.org/10.1017/CBO9781139021562.004.
Grégoire, V., Darrozes, J., Gaillot, P., Nédélec, A., Launeau, P., 1998. Magnetite grain shape fabric and distribution anisotropy vs rock magnetic fabric: a three-dimensional case study. J. Struct. Geol. 20 (7), 937–944.
Hargraves, R.B., Johnson, D., Chan, C.Y., 1991. Distribution anisotropy: the cause of AMS in igneous rocks? Geophys. Res. Lett. 18 (12), 2193–2196. https://doi.org/10.1029/91GL01777.
Hawkes, L., Hawkes, H.K., 1933. The Sandfell Laccolith and "Dome of Elevation.". Q. J. Geol. Soc. Lond. 89, 379–400.
Heap, M.J., Troll, V.R., Kushnir, A.R.L., Gilg, H.A., Collinson, A.S.D., Deegan, F.M., Darmawan, H., Seraphine, N., Neuberg, J., Walter, T.R., 2019a. Hydrothermal alteration of andesitic lava domes can lead to explosive volcanic behaviour. Nat. Commun. 10 (1), 5063. https://doi.org/10.1038/s41467-019-13102-8.
Heap, M.J., Tuffen, H., Wadsworth, F.B., Reuschlé, T., Castro, J.M., Schipper, C.I., 2019b. The Permeability Evolution of Tuffisites and Implications for Outgassing through Dense Rhyolitic Magma. J. Geophys. Res. Solid Earth, 2018JB017035. https://doi.org/10.1029/2018JB017035.
Heiken, G., Wohletz, K., Eichelberger, J., 1988. Fracture fillings and intrusive pyroclasts, Inyo Domes, California. J. Geophys. Res. 93 (B5), 4335–4350.
Hess, K.-U., Dingwell, D.D., 1996. Viscosities of hydrous leucogranitic melts: a non-Arrhenian model. Am. Mineral. 81, 1297–1300.
Hornby, A.J., Lavallée, Y., Kendrick, J.E., De Angelis, S., Lamur, A., Lamb, O.D., Rietbrock, A., Chigna, G., 2019. Brittle-Ductile Deformation and Tensile Rupture of Dome Lava during inflation at Santiaguito, Guatemala. J. Geophys. Res. Solid Earth 124 (10), 10107–10131. https://doi.org/10.1029/2018JB017253.
Isom, S.L., Andrews, G.D.M., Kenderes, S., Whittington, A.G., 2023. Brittle deformation in silicic lavas. Geosphere 19 (2), 431–448. https://doi.org/10.1130/GES02499.1.
Jelínek, V., 1978. Statistical processing of anisotropy of magnetic susceptibility measured on groups of specimens. Stud. Geophys. Geod. 22 (1), 50–62. https://doi.org/10.1007/BF01613632.
Jelínek, V., 1981. Characterization of the magnetic fabric of rocks. Tectonophysics 79 (3–4), T63–T67. https://doi.org/10.1016/0040-1951(81)90110-4.
Kameda, M., Kuribara, H., Ichihara, M., 2008. Dominant time scale for brittle fragmentation of vesicular magma by decompression. Geophys. Res. Lett. 35 (14) https://doi.org/10.1029/2008GL034530.
Kendrick, J.E., Lavallée, Y., Mariani, E., Dingwell, D.B., Wheeler, J., Varley, N.R., 2017. Crystal plasticity as an indicator of the viscous-brittle transition in magmas. Nat. Commun. 8 (1) https://doi.org/10.1038/s41467-017-01931-4.
Khan, M.A., 1962. The anisotropy of magnetic susceptibility of some igneous and metamorphic rocks. J. Geophys. Res. 67 (7), 2873–2885. https://doi.org/10.1029/JZ067i007p02873.
Kushnir, A.R.L., Martel, C., Champallier, R., Arbaret, L., 2017. In situ confirmation of permeability development in shearing bubble-bearing melts and implications for volcanic outgassing. Earth Planet. Sci. Lett. 458, 315–326. https://doi.org/10.1016/j.epsl.2016.10.053.
Lamur, A., Kendrick, J.E., Wadsworth, F.B., Lavallée, Y., 2019. Fracture healing and strength recovery in magmatic liquids. Geology 47 (3), 195–198. https://doi.org/10.1130/G45512.1.
Lavallée, Y., Benson, P.M., Heap, M.J., Flaws, A., Hess, K.-U., Dingwell, D.B., 2012. Volcanic conduit failure as a trigger to magma fragmentation. Bull. Volcanol. 74, 11–13. https://doi.org/10.1007/s00445-011-0544-2.
Liu, Y., Zhang, Y., Behrens, H., 2005. Solubility of H2O in rhyolitic melts at low pressures and a new empirical model for mixed H2O-CO2 solubility in rhyolitic melts. J. Volcanol. Geotherm. Res. 143 (1–3), 219–235. https://doi.org/10.1016/j.jvolgeores.2004.09.019.
Magnall, N., James, M.R., Tuffen, H., Vye-Brown, C., Schipper, C.I., Castro, J.M., Davies, A.G., 2018. The origin and evolution of breakouts in a cooling-limited rhyolite lava flow. doi: 10.1130/B31931.1.
Martin, E., Paquette, J.L., Bosse, V., Ruffet, G., Tiepolo, M., Sigmarsson, O., 2011. Geodynamics of rift-plume interaction in Iceland as constrained by new 40 Ar/ 39 Ar and in situ U-Pb zircon ages. Earth Planet. Sci. Lett. 311, 28–38. https://doi.org/10.1016/j.epsl.2011.08.036.
Mattsson, T., Burchardt, S., Almqvist, B.S.G., Ronchin, E., 2018. Syn-emplacement fracturing in the sandfell laccolith, eastern Iceland—implications for rhyolite intrusion growth and volcanic hazards. Front. Earth Sci. 6 https://doi.org/10.3389/feart.2018.00005.
Mattsson, T., Petri, B., Almqvist, B., McCarthy, W., Burchardt, S., Palma, J.O., Hammer, Ø., Galland, O., 2021. Decrypting magnetic Fabrics (AMS, AARM, AIRM) through the Analysis of Mineral Shape Fabrics and distribution Anisotropy. J. Geophys. Res. Solid Earth 126 (6). https://doi.org/10.1029/2021JB021895.
Moore, J.G., Rice, C.J., 1984. Chronology and character of the May 18, 1980 explosive eruptions of Mount St Helens. In: Explosive Volcanism : Inception, Evolution, and Hazards. National Academy Press, pp. 133–142.
Nelson, S.A., 1981. The possible role of thermal feedback in the eruption of siliceous magmas. J. Volcanol. Geotherm. Res. 11, 127–137.
Ogburn, S.E., Loughlin, S.C., Calder, E.S., 2015. The association of lava dome growth with major explosive activity (VEI ≥ 4): DomeHaz, a global dataset. Bull. Volcanol. 77 (5) https://doi.org/10.1007/s00445-015-0919-x.
Okumura, S., Nakamura, M., Nakano, T., Uesugi, K., Tsuchiyama, A., 2010. Shear deformation experiments on vesicular rhyolite: Implications for brittle fracturing, degassing, and compaction of magmas in volcanic conduits. J. Geophys. Res. 115 (B6), B06201 https://doi.org/10.1029/2009JB006904.
Óskarsson, B.V., Riishuus, M.S., 2013. The mode of emplacement of Neogene flood basalts in Eastern Iceland: Facies architecture and structure of the Hólmar and Grjótá olivine basalt groups. J. Volcanol. Geotherm. Res. 267, 92–118. https://doi.org/10.1016/j.jvolgeores.2013.09.010.
Padilla, A. J. de (2015). Elemental and Isotopic Geochemistry of Crystal-Melt Systems: Elucidating the Construction and Evolution of Silicic Magmas in the Shallow Crust, Using Examples from Southeast Iceland and Southwest USA. PhD Dissertation. Vanderbilt University.
Papale, P., 1999. Strain-induced magma fragmentation in explosive eruptions. Nature 397, 425–428.
Parfitt, EA, Wilson, L, 2008. Fundamentals of physical volcanology. Blackwell, Malden, Mass, p. 230.
Pistone, M., Cordonnier, B., Caricchi, L., Ulmer, P., Marone, F., 2015. The viscous to brittle transition in crystal- and bubble-bearing magmas. Front. Earth Sci. 3, 1–14. https://doi.org/10.3389/feart.2015.00071.
Richard, D., Scheu, B., Mueller, S.P., Spieler, O., Dingwell, D.B., 2013. Outgassing: Influence on speed of magma fragmentation. J. Geophys. Res. Solid Earth 118 (3), 862–877. https://doi.org/10.1002/jgrb.50080.
Riley, P., Tikoff, B., 2010. Tabular fracture clusters: Dynamic fracturing produced by volatile expulsion, Sierra Nevada Batholith, California. J. Struct. Geol. 32 (10), 1488–1499. https://doi.org/10.1016/j.jsg.2010.09.006.
Rochette, P., Aubourg, C., Perrin, M., 1999. Is this magnetic fabric normal? A review and case studies in volcanic formations. Tectonophysics 307, 219–234.
Rooyakkers, S.M., Stix, J., Berlo, K., Petrelli, M., Sigmundsson, F., 2021. Eruption risks from covert silicic magma bodies. Geological Society of America | GEOLOGY 49. https://doi.org/10.1130/G48697.1.
Rust, A.C., Cashman, K.V., 2004. Permeability of vesicular silicic magma: Inertial and hysteresis effects. Earth Planet. Sci. Lett. 228 (1–2), 93–107. https://doi.org/10.1016/j.epsl.2004.09.025.
Ryan, A.G., Russell, J.K., Heap, M.J., Kolzenburg, S., Vona, A., Kushnir, A.R.L., 2019. Strain-Dependent Rheology of Silicate Melt Foams: Importance for Outgassing of Silicic Lavas. J. Geophys. Res. Solid Earth 124 (8), 8167–8186. https://doi.org/10.1029/2019JB018099.
Sato, H., Fujii, T., Nakada, S., 1992. Crumbling of dacite dome lava and generation of pyroclastic flows at Unzen volcano. Nature 360, 664–666.

Saubin, E., Tuffen, H., Gurioli, L., Owen, J., Castro, J.M., Berlo, K., McGowan, E.M., Schipper, C.I., Wehbe, K., 2016. Conduit Dynamics in Transitional Rhyolitic activity Recorded by Tuffisite Vein Textures from the 2008–2009 Chaitén Eruption. Front. Earth Sci. 4, 59. https://doi.org/10.3389/feart.2016.00059.

Schipper, C.I., Castro, J.M., Tuffen, H., James, M.R., How, P., 2013. Shallow vent architecture during hybrid explosive-effusive activity at Cordón Caulle (Chile, 2011-12): evidence from direct observations and pyroclast textures. J. Volcanol. Geotherm. Res. 262, 25–37. https://doi.org/10.1016/j.jvolgeores.2013.06.005.

Schmiedel, T., Burchardt, S., Mattsson, T., Guldstrand, F., Galland, O., Palma, J.O., Skogby, H., 2021. Emplacement and Segment Geometry of Large, High-Viscosity Magmatic Sheets. Minerals 11, 1113. https://doi.org/10.3390/min11101113.

Schmiedel, T., Galland, O., Breitkreuz, C., 2017. Dynamics of Sill and Laccolith Emplacement in the Brittle Crust: Role of Host Rock Strength and Deformation Mode. J. Geophys. Res. Solid Earth 122 (11), 8860–8871. https://doi.org/10.1002/2017JB014468.

Schmiedel, T., Galland, O., Haug, T., Dumazer, G., Breitkreuz, C., 2019. Coulomb failure of Earth's brittle crust controls growth, emplacement and shapes of igneous sills, saucer-shaped sills and laccoliths. Earth Planet. Sci. Lett. 510, 161–172. https://doi.org/10.1016/j.epsl.2019.01.011.

Seaman, S.J., Dyar, M.D., Marinkovic, N., 2009. The effects of heterogeneity in magma water concentration on the development of flow banding and spherulites in rhyolitic lava. J. Volcanol. Geotherm. Res. 183 (3–4), 157–169. https://doi.org/10.1016/j.jvolgeores.2009.03.001.

Shields, J.K., Mader, H.M., Caricchi, L., Tuffen, H., Mueller, S., Pistone, M., Baumgartner, L., 2016. Unravelling textural heterogeneity in obsidian: Shear-induced outgassing in the Rocche Rosse flow. J. Volcanol. Geotherm. Res. 310, 137–158. https://doi.org/10.1016/j.jvolgeores.2015.12.003.

Smith, J.V., Miyake, Y., Oikawa, T., 2001. Interpretation of porosity in dacite lava domes as ductile-brittle failure textures. J. Volcanol. Geotherm. Res. 112 (1–4), 25–35. https://doi.org/10.1016/S0377-0273(01)00232-3.

Smith, R., Sammonds, P.R., Tuffen, H., Meredith, P.G., 2011. Evolution of the mechanics of the 2004-2008 Mt. St. Helens lava dome with time and temperature. Earth Planet. Sci. Lett. 307, 191–200. https://doi.org/10.1016/j.epsl.2011.04.044.

Sparks, R.S.J., 2003. Dynamics of magma degassing. Geol. Soc. Lond. Spec. Publ. 213 (1), 5–22. https://doi.org/10.1144/GSL.SP.2003.213.01.02.

Stephenson, A., 1994. Distribution anisotropy: two simple models for magnetic lineation and foliation. In *Physics of the Earth and Planetary Interiors* 82.

Tait, S., Jaupart, C., Vergniolle, S., 1989. Pressure, gas content and eruption periodicity of a shallow, crystallising magma chamber. Earth Planet. Sci. Lett. 92, 107–123.

Tarling, D.H., Hrouda, F., 1993. The Magnetic Anisotropy of Rocks. Chapman and Hall.

Tuffen, H., Castro, J.M., 2009. The emplacement of an obsidian dyke through thin ice: Hrafntinnuhryggur, Krafla Iceland. J. Volcanol. Geotherm. Res. 185 https://doi.org/10.1016/j.jvolgeores.2008.10.021.

Tuffen, H., Dingwell, D., 2005. Fault textures in volcanic conduits: evidence for seismic trigger mechanisms during silicic eruptions. Bull. Volcanol. 67 (4), 370–387. https://doi.org/10.1007/s00445-004-0383-5.

Tuffen, H., Dingwell, D.B., Pinkerton, H., 2003. Repeated fracture and healing of silicic magma generate flow banding and earthquakes? In Geology 3. https://pubs.geoscienceworld.org/gsa/geology/article-pdf/31/12/1089/3525964/i0091-7613-31-12-1089.pdf.

Tuffen, H., Smith, R., Sammonds, P.R., 2008. Evidence for seismogenic fracture of silicic magma. Nature Letters 453, 511–514. https://doi.org/10.1038/nature06989.

Tuffen, H., Farquharson, J.I., Wadsworth, F.B., Webb, C., Owen, J., Castro, J.M., Berlo, K., Schipper, C.I., Wehbe, K., 2022. Mid-loaf crisis: Internal breadcrust surfaces in rhyolitic pyroclasts reveal dehydration quenching. 50. https://doi.org/10.1130/G49959.1.

Twomey, V., 2023. The Interplay between Deformation and Magma Transport in Southeast Iceland. University of St Andrews. https://doi.org/10.17630/sta/318.

Unwin, H.E., Tuffen, H., Phillips, E., Wadsworth, F.B., James, M.R., 2021. Pressure-Driven opening and filling of a Volcanic Hydrofracture Recorded by Tuffisite at Húsafell, Iceland: a potential Seismic Source. Front. Earth Sci. 9 https://doi.org/10.3389/feart.2021.668058.

Vezzoli, L., Principe, C., Giordano, D., Felice, S. La, Landi, P., 2023. Physical Volcanology and Facies Analysis of Silicic Lavas: Monte Amiata Volcano (Italy). In *Updates in Volcanology*. https://doi.org/10.5772/intechopen.104012.

Wadsworth, F.B., Witcher, T., Vossen, C.E.J., Hess, K.U., Unwin, H.E., Scheu, B., Castro, J.M., Dingwell, D.B., 2018. Combined effusive-explosive silicic volcanism straddles the multiphase viscous-to-brittle transition. *Nature*. Communications 9 (1). https://doi.org/10.1038/s41467-018-07187-w.

Wadsworth, F.B., Witcher, T., Vasseur, J., Dingwell, D.B., Sheu, B., 2019. When does magma break? In: Gottsmann, J., Neuberg, J., Scheu, B. (Eds.), Advances in Volcanology: Volcanic Unrest, 1st ed. Springer, pp. 171–184. https://doi.org/10.1007/11157_2017_23.

Wadsworth, F.B., Llewellin, E.W., Castro, J.M., Tuffen, H., Schipper, C.I., Gardner, J.E., Vasseur, J., Foster, A., Damby, D.E., Mcintosh, I.M., Boettcher, S., Unwin, H.E., Heap, M.J., Farquharson, J.I., Dingwell, D.B., Iacovino, K., Paisley, R., Jones, C., Whattam, J., 2022. A reappraisal of explosive-effusive silicic eruption dynamics: syn-eruptive assembly of lava from the products of cryptic fragmentation. J. Volcanol. Geotherm. Res. 432, 107672 https://doi.org/10.1016/j.jvolgeores.2022.107672.

Walker, G.P.L., 1974. The structure of Eastern Iceland. In: Kristjansson, L. (Ed.), Geodynamics of Iceland and the North Atlantic Area, , Ed.vol. 11. D. Reidel Publishing Company, pp. 177–188.

Webb, S.L., Dingwell, D.B., 1990. The Onset of Non-Newtonian Rheology of Silicate Melts a Fiber Elongation Study. Phys. Chem. Miner. 17, 125–132.

Zierenberg, R.A., Schiffman, P., Barfod, G.H., Lesher, C.E., Marks, N.E., Lowenstern, J.B., Mortensen, A.K., Pope, E.C., Bird, D.K., Reed, M.H., Fridleifsson, G.Ó., Elders, W.A., 2013. Composition and origin of rhyolite melt intersected by drilling in the Krafla geothermal field, Iceland. Contrib. Mineral. Petrol. 165 (2), 327–347. https://doi.org/10.1007/s00410-012-0811-z.